Constraints from Phase Equilibrium Experiments on Pre-eruptive Storage Conditions in Mixed Magma Systems: a Case Study on Crystal-rich Basaltic Andesites from Mount Merapi, Indonesia

Saskia Erdmann, Caroline Martel, Michel Pichavant, Jean-Louis Bourdier, Rémi Champallier, J.-C. Komorowski, N. Cholik

Constraints from Phase Equilibrium Experiments on Pre-eruptive Storage Conditions in Mixed Magma Systems: a Case Study on Crystal-rich Basaltic Andesites from Mount Merapi, Indonesia

S. Erdmann[1]*, C. Martel[1], M. Pichavant[1], J.-L. Bourdier[1], R. Champallier[1], J.-C. Komorowski[2] and N. Cholik[3]

[1]Université d'Orléans–CNRS/INSU–ISTO–BRGM, UMR 7327, Orléans, France; [2]Equipe Systèmes Volcaniques, Institut de Physique du Globe de Paris, Sorbonne Paris-Cité, CNRS UMR-7154, Université Paris Diderot, Paris, France and [3]BPPTK (Balai Penyelidikan dan Pengembangan Tekonologi Kegunungapian), Yogyakarta, Indonesia

*Corresponding author: serdmann@dal.ca; phone: +33-02 38 25 53 83

Received July 8, 2015; Accepted March 31, 2016

ABSTRACT

Mount Merapi is one of Indonesia's and the world's most hazardous volcanoes. Existing constraints on the location and the crystallization conditions of its pre-eruptive magma reservoir based on mineral and glass thermobarometry and geophysical surveys are inconclusive, yet of immediate importance for future hazard mitigation. Here, we use two series of phase equilibrium experiments to quantify the conditions of pre-eruptive magma storage and magma recharge in Merapi's upper-crustal reservoir: (1) to characterize crystallization at total equilibrium conditions; (2) to characterize crystallization at local equilibrium conditions between crystal rims and host melt. We demonstrate that this experimental approach can constrain pre-eruptive crystallization conditions and their variation in crystal-rich, mixed magma systems, such as that of Merapi, for which standard crystallization experiments and mineral thermobarometry fail. In agreement with geophysical estimates, we infer that Mount Merapi's pre-eruptive reservoir partially crystallizes at $\geq$100–200 $\pm$ 75 MPa and thus at relatively shallow depths of *c.* $\geq$4·5 to $\sim$9 km. Magmas are stored at $\geq$925–950 $\pm$ 25°C with a melt H_2O content of $\sim$3–4 wt % and a vapour phase with an XH_2O [H_2O/($H_2O + CO_2$)] of $\sim$0·5–0·6 $\pm$ 0·1. Pre-eruptive recharge magmas, in contrast, have a temperature >950 to <1000°C, a higher melt H_2O content of $\sim$4–5 wt % and a vapour phase with a higher XH_2O of $\sim$0·8 $\pm$ 0·1. We hypothesize that these variations in melt H_2O content and vapour XH_2O between resident and pre-eruptive recharge magmas relate to variable degrees of open-system degassing of magma parcels en route into the reservoir rather than to variations in volatile fluxing of the stored magmas.

Key words: H_2O; CO_2; crystal-rich; experiment; magma mixing; Merapi; volatiles

INTRODUCTION

Constraining pre-eruptive magma storage conditions is of immediate importance for assessing hazard potential and hazard types at active volcanoes (Woods, 1995; Sparks, 2003; Scaillet *et al.*, 2008; Ruprecht & Bachmann, 2012; Cashman & Sparks, 2013), yet this is rarely achieved. Mount Merapi in Indonesia, one of the world's most hazardous volcanoes, is a prime example, for which pre-eruptive magma storage conditions are poorly constrained. The volcano rises above densely populated countryside and is located $\sim$30 km from the metropolis of Yogyakarta. On average, Merapi erupts

every few years. Its historical eruptions have been dominated by periods of lava dome growth and eventual gravitational dome collapse that typically produce VEI1 to VEI3 pyroclastic flows and surges (Voight *et al.*, 2000; Charbonnier & Gertisser, 2008; Gertisser *et al.*, 2011). These flows clearly affect the local population, but proficient hazard management has limited the number of fatalities. However, explosive VEI4 eruptions that affect a much larger area and population occasionally take place, as in 2010, and the rock record shows that such explosive events were more common in prehistoric times (Andreastuti *et al.*, 2000; Camus *et al.*, 2000; Gertisser *et al.*, 2011). For future hazard management it is thus imperative to (1) closely monitor the current pre-eruptive magma reservoir and (2) assess whether highly explosive eruptions will remain the exception, or whether they may become more common.

Geophysical surveys—including seismic, ground deformation, and magnetotelluric studies—have inferred shallow magma storage zones at depths of ~1·5–2·5 km and at >5 km to ~8·5 km below Merapi's summit; however, the shallowest zones may represent the presence of brines rather than magma storage zones (Ratdomopurbo & Poupinet, 1995, 2000; Beauducel & Cornet, 1999; Müller & Haak, 2004; Budi-Santoso *et al.*, 2013). Petrological studies and mineral barometry have suggested a wide range of possible crystallization pressures: (1) 0 to >600 MPa and predominantly ~100–400 MPa or ~400–500 MPa for clinopyroxene (Gertisser, 2001; Chadwick *et al.*, 2013; Preece *et al.*, 2014); (2) >300 to ~900 MPa and predominantly ~400–500 MPa for amphibole (Costa *et al.*, 2013; Nadeau *et al.*, 2013). Glass inclusion hygrobarometry and the evolved compositions of plagioclase and clinopyroxene indicate limited shallow magma storage at ≤300 MPa (Costa *et al.*, 2013; Nadeau *et al.*, 2013; Preece *et al.*, 2014). In combination, these calculated pressures suggest crystallization throughout the crust and upper mantle, with major magma crystallization zones at depths of ~4–18 km. Estimates for crystallization temperatures in the magma storage reservoir range widely from ~950°C using amphibole thermometry (Costa *et al.*, 2013; Erdmann *et al.*, 2014) to ~1050°C using clinopyroxene thermometry (Preece *et al.*, 2014). The limited data available indicate pre-eruptive melt H_2O contents between ~3·5 and 5·0 wt % (Borisova *et al.*, 2013; Preece *et al.*, 2014).

The aim of our study is to provide experimentally constrained estimates for the pre-eruptive crystallization conditions and processes in Merapi's current pre-eruptive magma storage reservoir and, in particular, constraints on the crystallization pressure and melt volatile content, which are key hazard factors. We anticipated that previous estimates of crystallization pressure and thus the location of the reservoir could be improved upon, given that they were inferred on the basis of amphibole and clinopyroxene mineral barometers with large uncertainties (Fig. 1).

By mimicking the crystallization conditions of natural magma systems, experimental studies can in principle provide highly accurate estimates for all intensive crystallization parameters. The challenge is, however, to constrain the crystallization conditions for mixed magma systems for which end-member magma compositions are not preserved in the rock record (Pichavant *et al.*, 2007; Blundy & Cashman, 2008). Merapi's crystal-rich, compositionally homogeneous basaltic andesites have been interpreted to represent a thorough mixture of relatively evolved resident and more primitive recharge magmas (Nadeau *et al.*, 2010, 2013; Chadwick *et al.*, 2013; Costa *et al.*, 2013), and thus they provide an excellent case study to address this challenge. To constrain the conditions in Merapi's pre-eruptive reservoir experimentally we needed to identify the natural equilibrium mineral assemblages and the crystallization conditions for the resident and the recharge magmas, respectively. To achieve this objective, we have (1) characterized the mixed mineral assemblages and their compositions in the eruption products of the paroxysmal 2010 eruption of Merapi and (2) performed two series of phase equilibrium experiments to quantify their record of crystallization conditions and processes during both magma storage and recharge.

SAMPLES, METHODS, AND DATA

The 2010 eruption of Merapi was its largest explosive event since 1872. For this VEI~4 event, eight eruption stages have been distinguished by Komorowski *et al.* (2013): stage 1, precursory unrest; stage 2, vulcanian or phreatomagmatic explosions; stage 3, rapid dome growth and vulcanian explosions; stage 4, paroxysmal, full dome and upper conduit explosion; stage 5, retrogressive old dome collapse; stage 6, convective column fountain collapse; stage 7, rapid dome growth and ash venting; stage 8, continuous ash venting. The stage 7 dome has remained largely intact since its emplacement in 2010, although ash plumes and small volumes of dome clasts were emitted from it in July and November 2013 and in March and April 2014.

We have studied 25 samples of the 2010 eruptive and dome-forming event including the following: (1) black, dense and glassy to scoriaceous dome clasts of stage 4; (2) white pumice of stage 6; (3) light to medium grey, dense to scoriaceous clasts derived from the terminal stage 7 dome. The stage 4 + 6 samples were collected by us in 2010 in Kali Gendol and near the tourist site at Mariam Bunker. The stage 7 samples were collected by S. Byrdina at Pasar Bubar on 19 November 2013, immediately following their eruption in a small explosion that occurred on 18 November 2013 through the dome that was emplaced on 6–8 November 2010 during stage 7. The stage 4 and stage 6 samples were selected because they represent the main erupted magma volume and the most explosive eruption stage, respectively. The stage 7 samples were studied because they have not been previously characterized; they represent the final magma emplaced during the 2010 eruption cycle, and we anticipated that they may yield

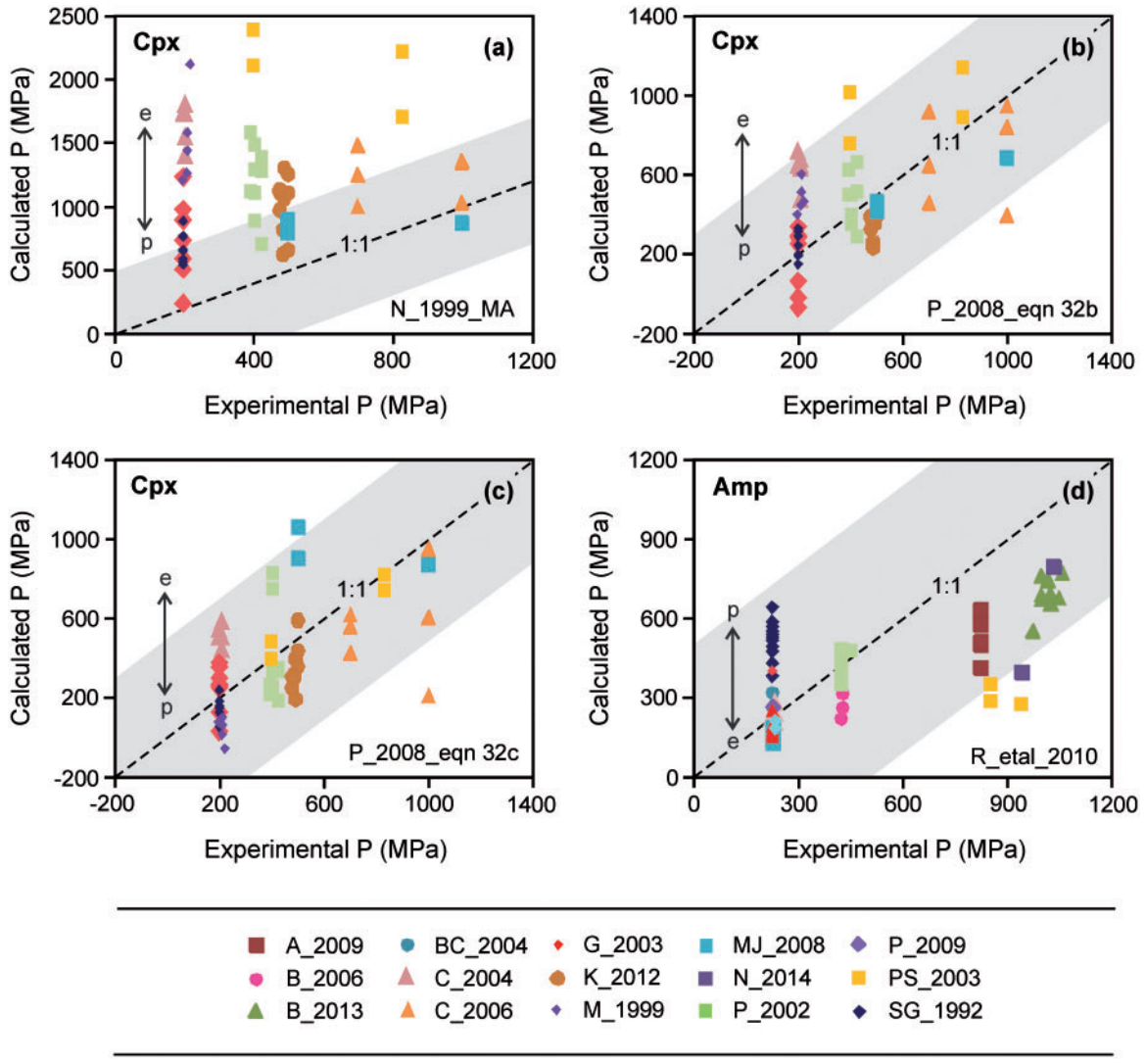

Fig. 1. Comparison of experimental and calculated crystallization pressures using the composition of (a–c) clinopyroxene and (d) amphibole crystallized from calc-alkaline magmas and the barometers of (a) Nimis (1999), mildly alkaline (MA) calibration; (b, c) Putirka [2008, equations (32b) and (32 c)]; and (d) Ridolfi *et al.* (2010). We note that Nimis (1999) explicitly discouraged the use of his barometer for clinopyroxene from calc-alkaline rocks. However, all the calibrations have been employed to estimate crystallization pressure for the Merapi magma plumbing system, even though they have large uncertainties of $\geq$260–500 MPa and systematic errors relating to compositional variations, increasing or decreasing with evolved (e) or primitive (p) magma, melt and mineral compositions as indicated by double-headed arrows. The grey shaded fields highlight calculated pressures within $\pm$ 500 MPa of the known experimental pressures. Detailed evaluations of the thermobarometric methods, their potential and problems have been given by Putirka (2008), Erdmann *et al.* (2014) and Stamper *et al.* (2014). Sources of experimental data: A_2009, Alonso-Perez *et al.* (2009); B_2006, Bogaerts *et al.* (2006); B_2013, Blatter *et al.* (2013); BC_2004, Barclay & Carmichael (2004); C_2004, Costa *et al.* (2004); C_2006, Caricchi *et al.* (2006); G_2003, Grove *et al.* (2003); K_2012, Krawczynski *et al.* (2012); M_1999, Martel *et al.* (1999); MJ_2008, Mercer & Johnston (2008); N_2014, Nandedkar *et al.* (2014); P_2002, Pichavant *et al.* (2002); P_2009, Pietranik *et al.* (2009); PS_2003, Prouteau & Scaillet (2003); SG_1992, Sisson & Grove (1992) (the dataset used is provided in Supplementary Data Electronic Appendix A1).

additional insight into the previously proposed, but cryptic pre-eruptive recharge of Merapi's upper magma system (e.g. Costa *et al.*, 2013). We are confident that the samples classified as stage 7 are derived from Merapi's terminal 2010 dome, because they have abundant calcic ($\geq$An60–70) plagioclase microlites that are characteristic for the magmas of the 2010 eruptive event, but are unknown from other recent eruption products (Costa *et al.*, 2013; Preece *et al.*, 2013). Magnetite phenocrysts in these samples show trellis-like exsolution, which is consistent with slow cooling (e.g. Turner *et al.*, 2008) during magma ascent and/or dome residence, but they show no or minor oxidation. In the following analysis we distinguish between stage 4 + 6 and stage 7 samples, based on variable proportions of evolved and inclusion-rich versus primitive and inclusion-poor phenocrysts. The dome clasts and pumice samples of stage 4 + 6, however, have phenocryst populations with comparable textures and compositions, and they are thus described together.

Five selected whole-rock samples (one stage 4 dome clast, four stage 7 dome clasts) were geochemically

Table 1: Composition of whole-rock (WR) and glass (Gl) starting material normalized to 100 wt %

St. mat.	SiO_2	TiO_2	Al_2O_3	Fe_2O_3	MnO	MgO	CaO	Na_2O	K_2O	P_2O_5	Total
WR* (100 wt %)	55·11	0·78	19·20	7·69	0·21	2·38	8·39	3·79	2·13	0·32	98·1†
Gl‡ (100 wt %)	57·19	0·69	18·32	6·86	0·12	2·36	8·28	3·81	2·12	0·25	98·9†

St. mat., starting material sample SEM043b.
*Analyzed by XRF at Saint Mary's University, Canada.
†Pre-normalized totals.
‡Analyzed by electron microprobe at ISTO, France.
The ~11% lower Fe_2O_3 content determined for the glass as compared with the whole-rock composition may partly reflect Fe loss during glass fusion. Apparent deviations in other element concentrations (e.g. ~4 and 5% for SiO_2 and Al_2O_3) between WR and Gl starting materials are considered to reflect analytical and method-related errors.

analyzed at the Regional Analytical Centre at Saint Mary's University, Canada, and 25 natural samples were studied in thin section. For our experimental study, we used one of the black, glassy, dense basaltic andesite stage 4 dome clasts (sample SEM043b) as the starting material (Table 1; Fig. 2). We have selected this starting material for the following reasons: (1) the sample represents the main clast type that was discharged in the high-volume pyroclastic flows on 5 November 2010 [i.e. it is a Type 1 clast following the classification of Charbonnier *et al.* (2013), which make up >61 to 84 vol. % and on average 77 vol. % of all stage 4 pyroclasts]; (2) the sample has a whole-rock composition close to the average of all juvenile pyroclasts erupted in 2010 (Fig. 2); (3) the sample has a phenocryst and microphenocryst assemblage of plagioclase–clinopyroxene–orthopyroxene–amphibole–magnetite, which is characteristic of Merapi basaltic andesites (Fig. 3a and b); (4) the sample has mineral rim compositions similar to those of other stage 4 pyroclasts and stage 6 pumice samples investigated (Figs 2 and 4c, g, k; Supplementary Data Electronic Appendix A2; supplementary data are available for downloading at http://www.petrology.oxfordjournals.org).

For one series of experiments, referred to as 'melting experiments', we have used a gently crushed powder of the crystal-rich basaltic andesite whole-rock, which was partially melted and partially recrystallized during the experiments. For the second series of experiments, referred to as 'crystallization experiments', we have fused the same rock powder to a homogeneous glass at atmospheric conditions, which was then partially crystallized during the experiments. The melting experiments were performed to characterize the local equilibrium compositions of crystal rims and their host melts for Merapi's crystal-rich basaltic andesites (i.e. accounting for the fact that crystal cores of Merapi's mixed mineral assemblage are not in equilibrium) (Table 2). The crystallization experiments were performed to provide phase compositions that form at equilibrium for the basaltic andesite composition (Table 2), which guided our interpretation of the mineral rim compositions detected in the melting experiments. For both experimental series, Au capsules were first loaded with variable amounts of ultrafiltered, deionized H_2O and silver oxalate ($Ag_2C_2O_4 \rightarrow CO_2$) to yield equilibrium with a vapour phase with an XH_2O [$H_2O/(H_2O + CO_2)$] between ~0·4 and 1 (Table 3), and then filled with the starting rock or starting glass powders at a fluid:solid ratio of ~1:10 to impose volatile-saturated conditions as in Merapi's mid- to upper-crustal magma system (see Nadeau *et al.*, 2010, 2013).

The two series of experiments were run simultaneously in internally heated pressure vessels at the Institut des Sciences de la Terre d'Orléans (ISTO), France. The oxygen fugacity (fO_2) was controlled by loading ~1 bar of H_2 into the vessels, except for one experiment that was performed at the intrinsic fO_2 of the vessel at >NNO + 2 (where NNO is the nickel–nickel oxide buffer) (CE-1, Table 2). The fO_2 was monitored by a pair of NiO + Ni–Pd solid sensors (see Pownceby & O'Neill, 1994), which indicate that the fO_2 of the experiments with H_2 added reached ~NNO + 1·5 to ~NNO + 1·3 in charges with an $XH_2O_V = 1$, and the fO_2 was ~NNO + 0·9 to ~NNO + 0·7 in charges with an XH_2O_V of ~0·6–0·5 (Table 3). The experimental pressure and temperature were then induced by loading Ar into the vessel, followed by heating at a rate of 10–15°C min^{-1}. At the beginning of each experiment, we overstepped the targeted experimental temperature by ~40°C for 2–3 h to promote partial melting and subsequent crystallization of mineral rims that were wide enough for analysis. All experiments were run for ~3 days at 925–1000°C and ~100–400 MPa (Table 3), and ended by drop quench. Temperature and total pressure were continuously monitored; their uncertainties are ± 5°C and ± 2 MPa.

For the natural samples, we distinguish between phenocrysts (>500 μm), microphenocrysts (~100–500 μm) and microlites (>500 μm). For the melting experiments, we distinguish between unreacted crystal cores and newly crystallized inner and outer mineral rims. Mineral proportions in the experimental and natural samples were determined by point counting on backscattered electron images and thin sections, respectively. Mineral, matrix and glass compositions were determined by electron microprobe at ISTO. Average and representative mineral and glass compositional data for the natural samples and the experimental charges are provided in Supplementary Data Electronic Appendices A2 and A3. For the natural samples we determined the phenocryst core and rim compositions for 10 samples and the matrix

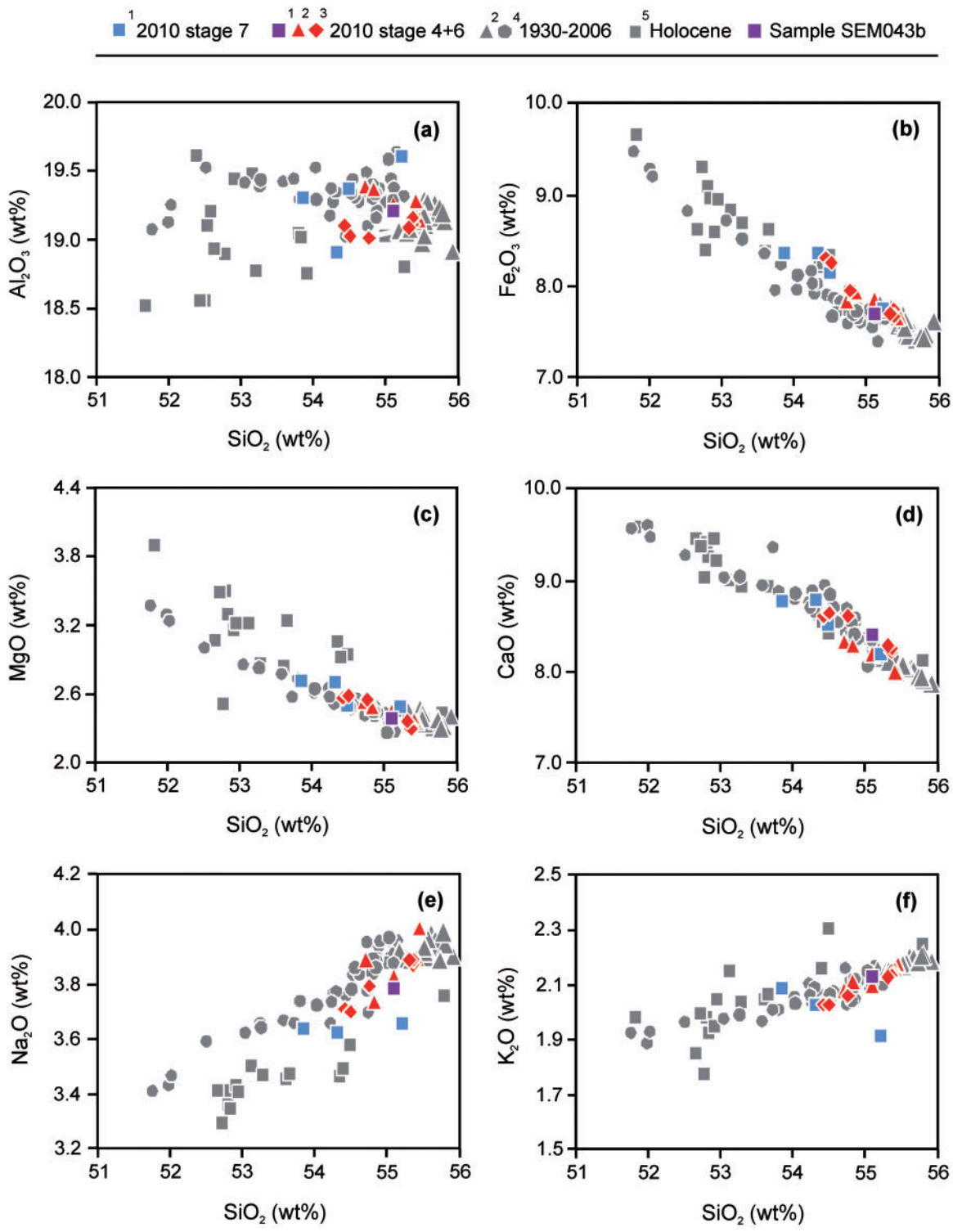

Fig. 2. Major-element compositional variations of Merapi whole-rocks normalized to 100 wt % anhydrous. The stage 4 + 6 samples (erupted on 5 November) and the stage 7 samples (of the terminal 2010 dome, which were erupted on 18 November 2013) have basaltic andesite compositions, notably lacking a juvenile basaltic component. Data sources: (1) this study; (2) Preece *et al.* (2013); (3) Costa *et al.* (2013); (4) Abdurachman (1998); (5) Gertisser & Keller (2003). Sample SEM043b is the sample that was used as the starting material for our experiments.

and glass inclusion compositions for six samples. For the crystallization experiments, we determined mineral and glass compositions for key charges. For the melting experiments, we determined mineral rim and glass compositions whenever they were large enough for analysis. The electron microprobe operating conditions were set at 15 keV and 10 nA with peak and background counting times of 10–20 s. All minerals were analyzed with a

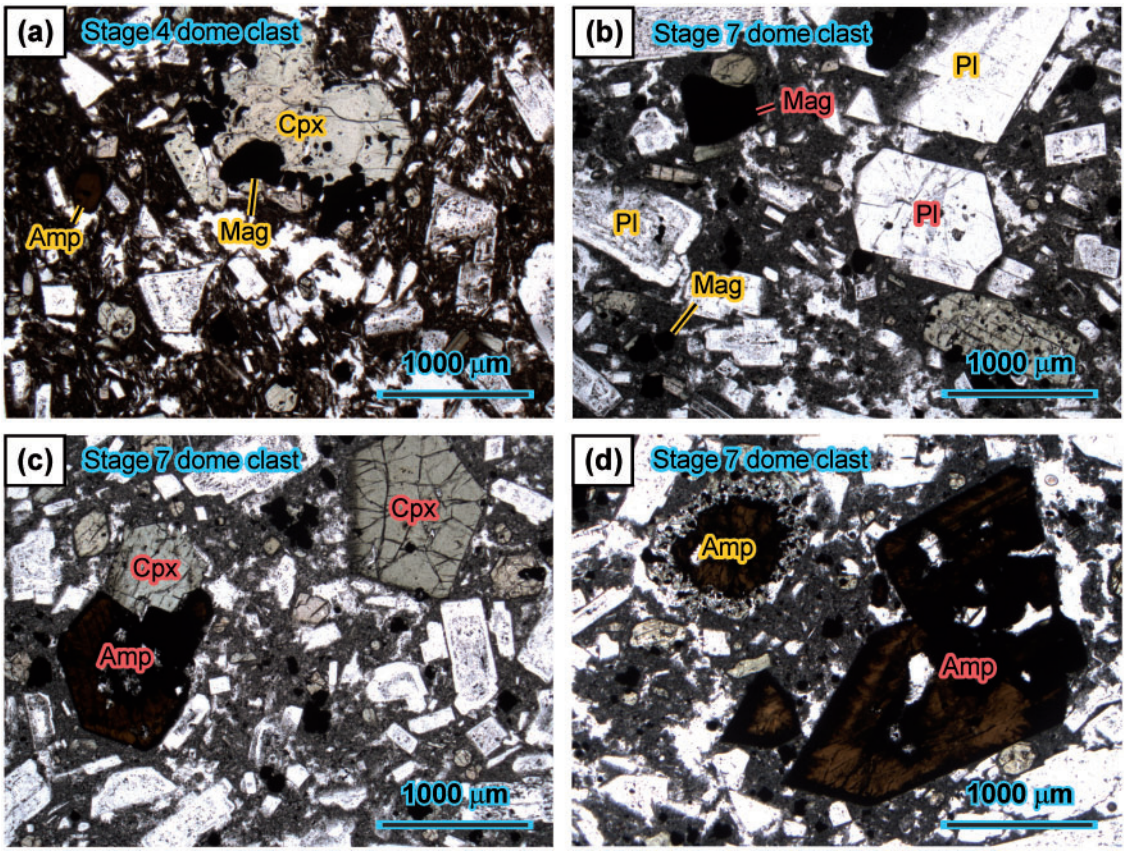

Fig. 3. Photomicrographs of typical (a) stage 4 and (b–d) stage 7 samples from the Merapi 2010 eruptive event. All are basaltic andesitic, crystal-rich, and dense dome clasts. Crystals with inclusion-rich zones, resorption features, complex oscillatory zoning and/or evolved compositions form the main assemblages in all samples. Typical examples are highlighted by yellow labels. Crystals with few inclusions, normal zoning and primitive core compositions are more abundant in the stage 7 than in the stage 4 + 6 samples. Typical examples are highlighted by red labels.

focused beam; the experimental and the natural glasses and matrix compositions were analyzed using defocused 20 μm and 50 μm beam diameters, respectively. We analyzed both glass inclusions and the matrix because we anticipated that the matrix compositions would provide a more complete record of pre-eruptive melt compositions and compositional variation. The matrix analyses intentionally included glass domains and microlites, because they were performed to characterize the melt present in the pre-eruptive reservoir prior to microlite crystallization. Alkali migration in glasses under the electron beam was corrected for relative to the hydrous glass standards of Scaillet & Evans (1999). Glass volatile contents, which primarily represent glass H_2O contents, were estimated relative to the hydrous glass standards and electron microprobe totals with an uncertainty of *c.* ± 1 wt %. Glass H_2O and CO_2 contents were also calculated using VolatileCalc (Newman & Lowenstern, 2002) for an average of predicted volatile solubilities in rhyolitic and basaltic melts (to account for the dacitic melt compositions in Merapi's magma reservoir). The uncertainties on the calculated solubilities are typically better than ± 1 wt % for H_2O, but up to ± 1000 ppm for CO_2, whereas relative uncertainties on CO_2 solubilities at <500 MPa and in a vapour with an XH_2O of ≤0·5 are <200 ppm (see Baker & Alletti, 2012). Because the calculated glass volatile and glass H_2O contents closely compare (Table 3), and glass volatile contents could not be determined for all experimental charges, we predominantly refer to the calculated melt H_2O contents in subsequent text and figures. The vapour XH_2O compositions (XH_2O_V) reported throughout the text and figures are those that prevailed once the experimental melts had reached volatile saturation and the charges had reached equilibrium ($XH_2O_V = XH_2O_{eq}$; Table 3).

Reported mineral end-member compositions are percentage anorthite {An = [Ca/(Ca + Na + K)] × 100} and orthoclase {Or = [K/(K + Ca + Na)] × 100} for plagioclase, enstatite {En = [Mg/(Mg + Fe_{tot} + Ca)] × 100}, wollastonite {Wo = [Ca/(Ca + Mg + Fe_{tot})] × 100} and ferrosilite {Fs = [Fe_{tot}/(Ca + Mg + Fe_{tot})] × 100} for clinopyroxene and orthopyroxene, and forsterite {Fo = [Mg/(Mg + Fe_{tot})] × 100} for olivine. Normal and reverse zoning refer to rimward decreasing or increasing Ca, Al, or Mg contents, respectively. Mineral–melt partition coefficients (K_D) are $(Ca/Na)_{Pl}/(Ca/Na)_{Gl}$ for plagioclase and $(Fe/Mg)_{Pl}/(Fe/Mg)_{Gl}$ for clinopyroxene, which are reported as average values for single charges. The mineral abbreviations used in text and figures follow those of Whitney & Evans (2010).

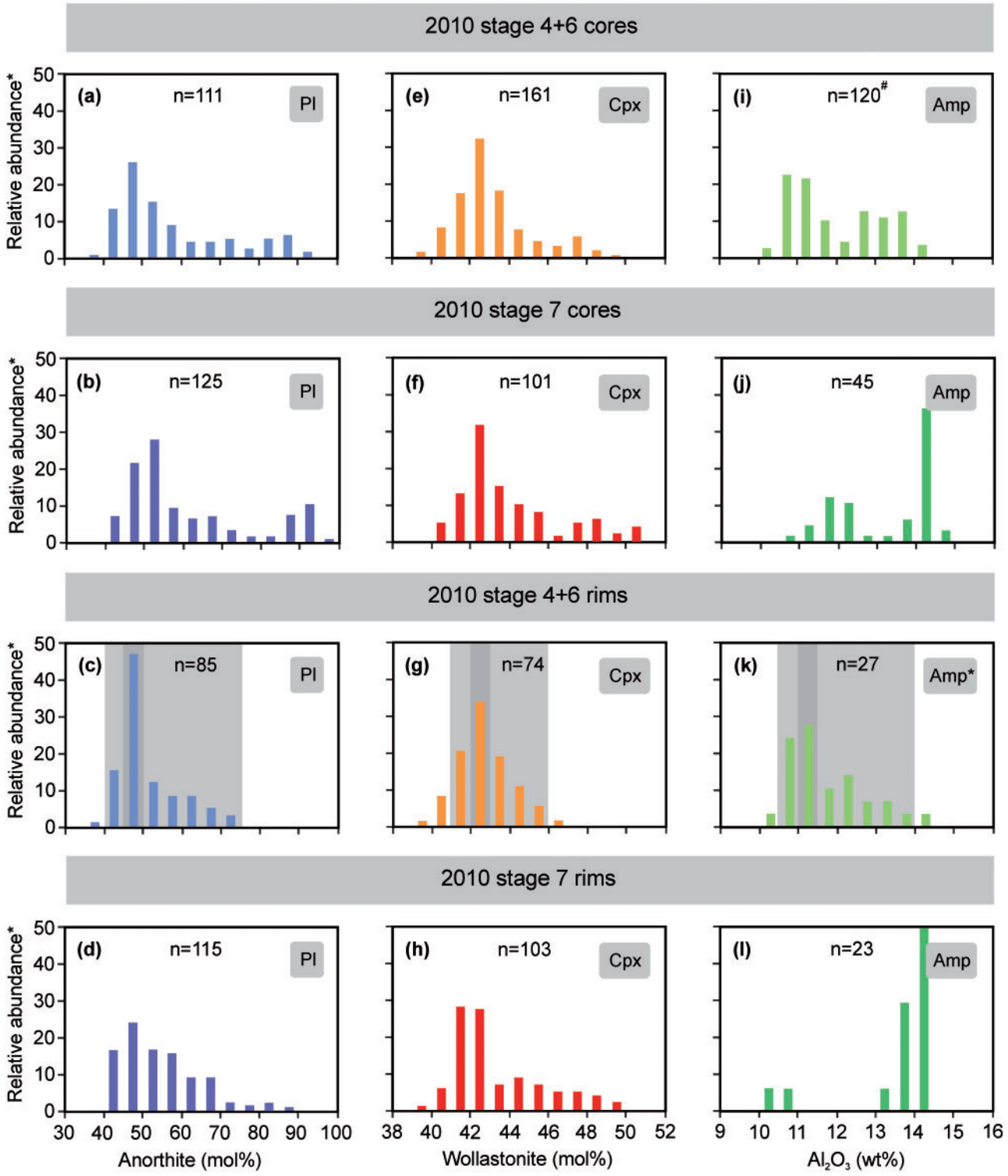

Fig. 4. Summary of the compositional variation for (a–d) plagioclase, (e–h) clinopyroxene, and (i–l) amphibole core and rim compositions in stage 4 + 6 and stage 7 samples. The core compositions are bimodal; the rim compositions show a wide range of compositions in which primitive compositions are slightly more common in the stage 7 than in the stage 4 + 6 samples. *, abundance normalized to 100; *n*, number of original analyses; #, data from Erdmann *et al.* (2014). Dark and light grey shaded fields in (c), (g), and (k) show the mode and range of outer mineral rim compositions for our starting material sample SEM043b.

Table 2: Possible experimental and natural equilibrium states

Total equilibrium = equilibrium for all phases and chemical components of the system
Local equilibrium = equilibrium for all crystal rims and host melt, but not for crystal cores and host melt
Partial equilibrium = equilibrium for some, but not all crystal rims and host melt

Table 3: Conditions and run products of crystallization experiments (CE) and melting experiments (ME)

Exp.	Charge (vol. %)	XH_2O_{in}* (wt %)	XH_2O_{eq}† (wt %)	ΔNNO‡ (ppm)	Phase assemblage	ϕ	Melt V§	Melt H_2O¶	Melt CO_2¶
Run 10: 99 MPa, 950° C, fH_2 = 1 bar, t = 85 h									
CE-10	10–36 c	1·00	1·00	1·5	Gl, Pl, Cpx, Mag	36	—	3·3	0
CE-10	10–38 c	0·80	0·76	1·3	Gl, Pl, Cpx, Mag	50	—	2·8	130
CE-10	10–37 c	0·73	0·68	1·2	Gl, Pl, Cpx, Mag, Opx	60	—	2·6	180
CE-10	10–39 c	0·60	0·55	1·0	Gl, Pl, Cpx, Mag, Opx	75	—	2·3	240
CE-10	10–41 c	0·56	0·51	0·9	Gl, Pl, Cpx, Mag, Opx	87	—	2·2	270
ME-10	10–20 m	1·00	1·00	1·5	Gl, Pl, Cpx, Mag	40	3·8	3·3	0
ME-10	10–21 m	0·80	0·77	1·3	Gl, Pl, Cpx, Mag, Opx	52	3·5	2·8	120
ME-10	10–22 m	0·63	0·56	1·0	Gl, Pl, Cpx, Mag, Opx	58	2·9	2·4	240
ME-10	10–23 m	0·53	0·48	0·9	Gl, Pl, Cpx, Mag, Opx	65	2·5	2·1	290
Run 9: 202 MPa, 925° C, fH_2 = 1 bar, t = 80 h									
CE-9	9–31 c	1·00	1·00	1·5	Gl, Pl, Cpx, Mag	40	—	4·9	0
CE-9	9–32 c	0·81	0·75	1·3	Gl, Pl, Cpx, Mag	52	—	4·0	280
CE-9	9–34 c	0·62	0·58	1·0	Gl, Pl, Cpx, Mag	80	—	3·4	480
CE-9	9–35 c	0·56	0·54	0·9	Gl, Pl, Cpx, Mag	90	—	3·3	520
ME-9	9–16 m	1·00	1·00	1·5	Gl, Pl, Cpx, Mag, Amp	43	5·3	4·9	0
ME-9	9–17 m	0·81	0·75	1·3	Gl, Pl, Cpx, Mag, Amp	49	4·8	4·0	290
ME-9	9–18 m	0·62	0·54	1·0	Gl, Pl, Cpx, Mag	62	4·0	3·3	520
ME-9	9–19 m	0·56	0·49	0·9	Gl, Pl, Cpx, Mag	70	3·8	3·0	590
Run 7: 204 MPa, 950° C, fH_2 = 1 bar, t = 70 h									
CE-7	7–26 c	1·00	1·00	1·3	Gl, Pl, Cpx, Mag	25	5·5	4·8	0
CE-7	7–27 c	0·90	0·86	1·2	Gl, Pl, Cpx, Mag	42	5·2	4·3	140
CE-7	7–29 c	0·72	0·66	0·9	Gl, Pl, Cpx, Mag	66	3·8	3·6	360
CE-7	7–30 c	0·60	0·56	0·8	Gl, Pl, Cpx, Mag	80	—	3·2	460
ME-7	7–13 m	1·00	1·00	1·3	Gl, Pl, Cpx, Mag	35	5·3	4·8	0
ME-7	7–15 m	0·64	0·55	0·8	Gl, Pl, Cpx, Mag	55	3·1	3·2	470
Run 6: 195 MPa, 1000° C, fH_2 = 1 bar, t = 67 h									
CE-6	6–11 c	1·00	1·00	1·3	Gl, Pl, Cpx	7	—	4·8	0
CE-6	6–12 c	0·90	0·85	1·2	Gl, Pl, Cpx, Mag	30	—	4·2	150
CE-6	6–13 c	0·81	0·74	1·0	Gl, Pl, Cpx, Mag	48	—	3·9	260
CE-6	6–14 c	0·72	0·65	0·9	Gl, Pl, Cpx, Mag	60	—	3·7	340
CE-6	6–15 c	0·63	0·57	0·8	Gl, Pl, Cpx, Mag	72	—	3·3	430
ME-6	6–7 m	1·00	1·00	1·3	Gl	0	—	4·8	0
ME-6	6–8 m	0·81	0·73	1·0	Gl, Pl, Cpx, Mag	35	4·4	3·9	270
ME-6	6–9 m	0·62	0·51	0·7	Gl, Pl, Cpx, Mag	50	3·4	3·1	480
Run 5: 295 MPa, 975° C, fH_2 = 1 bar, t = 67 h									
CE-5	5–16 c	1·00	1·00	1·5	Gl	0	—	6·4	0
CE-5	5–17 c	0·90	0·83	1·3	Gl, Pl, Cpx, Mag	36	—	5·6	280
CE-5	5–18 c	0·82	0·72	1·2	Gl, Pl, Cpx, Mag	43	—	5·0	480
CE-5	5–19 c	0·71	0·61	1·1	Gl, Pl, Cpx, Mag	58	—	4·5	640
CE-5	54–20 c	0·63	0·54	1·0	Gl, Pl, Cpx, Mag	70	—	4·1	750
ME-5	5–4 m	1·00	1·00	1·5	Gl	0	6·4	6·4	0
ME-5	5–5 m	0·81	0·71	1·2	Gl, Pl, Cpx, Mag	42	5·5	5·0	480
ME-5	5–6 m	0·63	0·47	0·9	Gl, Pl, Cpx, Mag	49	4·4	3·8	860
Run 8: 390 MPa, 1000° C, fH_2 = 1 bar, t = 72 h									
CE-8	8–21 c	1·00	1·00	1·4	Gl	0	8·7	7·9	0
CE-8	8–23 c	0·80	0·61	1·0	Gl, Pl, Cpx, Mag	27	5·5	5·5	900
CE-8	8–24 c	0·71	0·49	0·8	Gl, Pl, Cpx, Mag	38	4·5	4·7	1140
CE-8	8–25 c	0·62	0·46	0·7	Gl, Pl, Cpx, Mag	54	—	4·3	1220
ME-8	8–11 m	0·81	0·61	1·0	Gl, Pl, Cpx	27	6·0	5·4	890
ME-8	8–12 m	0·62	0·42	0·7	Gl, Pl, Cpx, Mag	44	4·7	4·1	1320
Run 1: 200 MPa, 975° C, fH_2 = 0 bar, t = 79 h									
CE-1	1–6 c	1·00	1·00	>2–3**	Gl, Pl, Cpx, Mag	16	—	4·9	0
CE-1	1–8 c	0·81	0·75	>2–3**	Gl, Pl, Cpx, Mag	49	—	4·0	270
CE-1	1–9 c	0·72	0·66	>2–3**	Gl, Pl, Cpx, Mag	63	—	3·7	360
CE-1	1–10 c	0·63	0·59	>2–3**	Gl, Pl, Cpx, Mag	76	—	3·4	450

*$XH_2O_{in} = H_2O/(H_2O + CO_2)$ (mol %) added to the charges.
†XH_2O_{eq} = final XH_2O of the experiment, calculated from XH_2O_{in}, melt H_2O solubilities, and experimental glass proportions; XH_2O_V reported in text corresponds to XH_2O_{eq}.
‡log fO_2 (experiment) – log fO_2 (NNO), where fO_2 in experiments was calculated from solid NiO + Ni–Pd sensors for variable XH_2O of the charges.
§Melt V is total melt volatile content, estimated by difference from electron microprobe totals and corrected relative to hydrous glass standards.
¶Calculated using VolatileCalc of Newman & Lowenstern (2002), where summarized H_2O and CO_2 contents are rounded values; estimated uncertainties are high; that is, up to ~1000 ppm (see Baker & Alletti, 2012).
**Intrinsic fO_2 of the pressure vessel (see Scaillet & Evans, 1999).
Exp., experiment; CE, crystallization experiment; ME, melting experiment; ϕ, crystallinity; Gl, glass; Pl, plagioclase; Cpx, clinopyroxene; Opx, orthopyroxene; Mag, magnetite; Amp, amphibole.

RESULTS

The natural samples

Whole-rock composition and petrology

Magmas that have erupted at Merapi in prehistoric to historical times are predominantly basaltic andesite in composition, but occasionally include basalts (Abdurachman, 1998; Gertisser & Keller, 2003; Chadwick *et al.*, 2013; Costa *et al.*, 2013; Preece *et al.*, 2013; Fig. 2). Their SiO_2 contents correlate poorly with Al_2O_3 (Fig. 2a), negatively correlate with MgO, Fe_2O_3 CaO and TiO_2 (Fig. 2b–d), and positively correlate with Na_2O and K_2O (Fig. 2e and f). The stage 4 + 6 samples erupted in 2010 and the stage 7 samples of the final 2010 dome have moderately evolved basaltic andesite compositions with ~53·9–55·4 wt % SiO_2 and ~18·9–19·6 wt % Al_2O_3, comparable with those of the majority of magmas discharged at Merapi from 1930 to 2006 (Abdurachman, 1998; Gertisser & Keller, 2003; Costa *et al.*, 2013; Preece *et al.*, 2013; Fig. 2). Basaltic magmas or enclaves, however, did not erupt in 2010 (stage 4 + 6) or in 2013 from the terminal 2010 dome (stage 7). Calc-silicate xenoliths are scarce (≪1 vol. %) and none of the samples is enriched in CaO. The compositions of the stage 4 + 6 and 7 samples are broadly comparable, but the stage 7 samples extend on average to slightly more primitive compositions with ~54·7 wt % SiO_2 relative to the stage 4 + 6 samples with ~55 wt % SiO_2 (Fig. 2a).

The investigated rocks, including dense and scoriaceous dome clasts and pumice samples, are crystal-rich with ~40–60 vol. % phenocrysts and microphenocrysts (Fig. 3). Plagioclase (~25–40 vol. %) and clinopyroxene (~5–15 vol. %) form the following: (1) common phenocrysts with complex zoning patterns, evidence of resorption, and inclusion-rich zones (Fig. 3a–c); (2) microphenocrysts that are largely inclusion-free (Fig. 3a–d); (3) rare phenocrysts that are inclusion-poor and largely unresorbed with core–rim step zoning (Fig. 3b–d). Magnetite (≤5 vol. %), amphibole (≤5 vol. %), and orthopyroxene (≤2 vol. %) are minor constituents that form subhedral to euhedral crystals (Fig. 3a–d). Olivine rarely occurs as inclusions <20 μm in size, most commonly in amphibole phenocrysts. The stage 4 + 6 samples characteristically have few inclusion-poor plagioclase and clinopyroxene phenocrysts with simple core–rim zoning (typically < 5 vol. %); they contain abundant subhedral, but few euhedral magnetite crystals (Fig. 3a). Largely unresorbed amphibole microphenocrysts are common, whereas unresorbed amphibole phenocrysts are absent (Fig. 3a). Most of the stage 7 samples, in contrast, have a larger proportion of inclusion-poor plagioclase and clinopyroxene crystals with simple core–rim zoning (typically ~5–15 vol. %), and euhedral magnetite crystals (Fig. 3b). They also have largely unresorbed amphibole phenocrysts in addition to microphenocrysts (Fig. 3d).

Mineral composition and zoning

Plagioclase, clinopyroxene, and amphibole in the basaltic andesites show a large range in composition, in which primitive core and rim compositions slightly increase in abundance from stage 4 + 6 to stage 7 samples (Fig. 4; Supplementary Data Electronic Appendix A2). Plagioclase has ~An40–90 core compositions with compositional maxima at ~An50 and ~An90, where the primitive >An80 compositions are characteristic of inclusion-poor crystal cores (Fig. 4a and b). The crystal rims have predominantly ~An50 to ~An70 composition, but range from ~An40 to ~An90 (Fig. 4c and d). Clinopyroxene is augite and less commonly diopside in composition, where cores (Fig. 4e and f) and rims (Fig. 4g and h) have ~Wo40–50 content with compositional maxima around ~Wo42–43. The core–rim zoning patterns of plagioclase and clinopyroxene include normal and reverse zoning, but zoning is most commonly irregularly oscillatory (Fig. 5). Broad plateau zones with evolved composition (i.e. typically with ~An40–50 and ~Wo42–43) and ~10–100 μm wide zones with intermediate composition (i.e. with ≤An70 and ≤Wo50) alternate. The outer ~100 μm of the crystals most commonly show normal zoning, but reverse zoning is

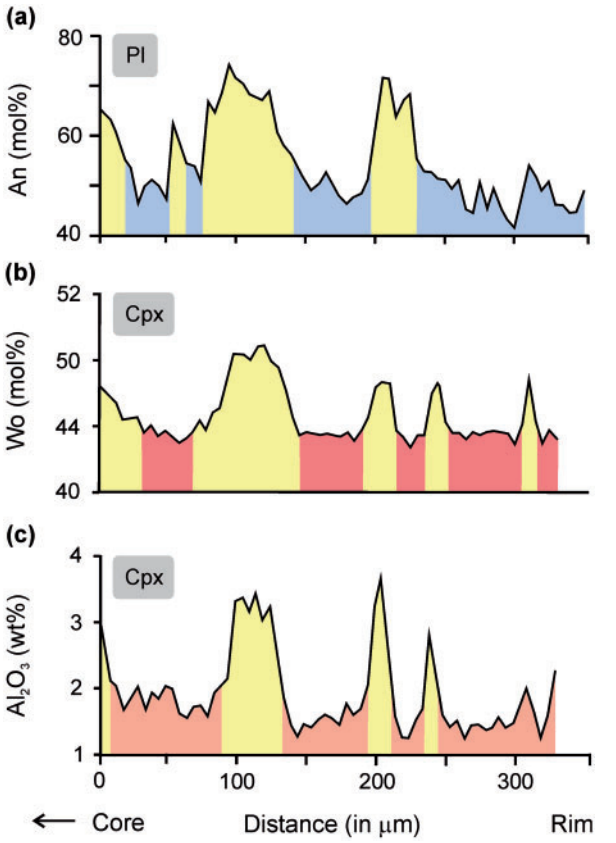

Fig. 5. Typical zoning profiles for (a) anorthite (An) in plagioclase, (b) wollastonite (Wo) and (c) Al_2O_3 in clinopyroxene from a stage 4 dome clast [same profile in (b) and (c)]. Characteristic features are (1) the evolved plateau zones with ~An50 plagioclase and ~Wo42–43 and ~2 wt % Al_2O_3 in clinopyroxene, and (2) the irregular and relatively thin, intermediate zones with <An70 in plagioclase and ≤Wo50 and <6 wt % Al_2O_3 in clinopyroxene.

also developed, particularly for plagioclase and clinopyroxene of the stage 7 samples.

Amphibole microphenocrysts in stage 4 + 6 samples have core compositions with ~11 and ~13 wt % Al_2O_3 (Fig. 4i). The crystals are normally or reversely zoned with rim compositions of ~10–14 wt % Al_2O_3 (Fig. 4k). Amphibole phenocrysts that are characteristic for the stage 7 samples are Al-rich compared with the microphenocrysts of the stage 4 + 6 samples, with compositional maxima at ~12 and 14 wt % Al_2O_3 (Fig. 4j). The cores with ~12 wt % Al_2O_3 often have patchy zoning and small olivine inclusions. The cores of the volumetrically predominant phenocryst type with ~14 wt % Al_2O_3 are largely unzoned except for low-amplitude oscillatory zoning and <200 μm wide normally zoned rims. The rims of the stage 7 phenocrysts and core or rim compositions of the stage 7 microphenocrysts were not analyzed, because they are pervasively oxidized. The near-rim compositions of the phenocrysts are, however, predominantly Al-rich with ~14 wt % Al_2O_3 (Fig. 4l), overlapping with the core and rim compositions of the most primitive stage 4 + 6 microphenocrysts (Fig. 4i and k).

Magnetite with subhedral shape, which is predominant in the stage 4 + 6 and the stage 7 samples, has core compositions with ~77 wt % FeO, ~2·7 wt % Al_2O_3 and ~8·8 wt % TiO_2. The crystals in the stage 4 + 6 samples are reversely zoned with rim compositions of ~76 wt % FeO, ~2·6–4·0 wt % Al_2O_3, and ~7·0–9·2 wt % TiO_2, whereas those in the stage 7 samples show trellis-like exsolution that has overprinted any original zoning. The rare euhedral magnetite crystals, which are characteristic for the stage 7 samples, have ~74 wt % FeO, ~6·0 wt % Al_2O_3 and ~5·6 wt % TiO_2 core composition, but their original zoning is also not preserved, owing to exsolution. Orthopyroxene, which predominantly occurs as microphenocrysts, has ~En67 core composition and is largely unzoned. Olivine, which occurs only in the form of inclusions, has an evolved ~Fo60–70, low NiO (<0·25 wt %), and high MnO (~1·0–1·4 wt %) and CaO (~0·1–0·2 wt %) composition.

Matrix and glass inclusion compositions

The matrix (glass plus microlites, analyzed with a 50 μm beam diameter) of the stage 4 + 6 and the stage 7 dome clasts is dacitic with ~66–70 wt % SiO_2, ~15–17 wt % Al_2O_3, and ~2–4 wt % CaO (Fig. 6). Glass inclusions in clinopyroxene phenocrysts have the same range of SiO_2 and Al_2O_3 contents as the matrix (Fig. 6a), but they have lower CaO contents of <2 wt %, indicating that they were modified by post-entrapment crystallization (Fig. 6b). Their volatile contents calculated by difference from electron microprobe totals are ~0·5–2·5 wt % for dome clasts and ~3–4 wt % for pumice samples.

The experimental study

Run products of the crystallization experiments

The seven crystallization experiments were carried out at 925–1000°C and ~100–400 MPa (Table 3). Six experiments were performed at moderately oxidizing conditions of ~NNO + 1·5 to ~NNO + 0·7; one experiment was performed at >NNO + 2 (CE-1) (Table 3). The crystallization of charges with an XH_2O_V of 1 to ~0·5 produced up to ~90 vol. % of euhedral to subhedral crystals. Crystallinities of ≤40–60 vol. %, which are characteristic for the natural samples, formed in charges crystallized at ≤950°C with an XH_2O_V of ≥0·7 and in charges crystallized at ≥975°C with an XH_2O_V of ≤0·8 (Table 3). Plagioclase (7–66 vol. %), clinopyroxene (0–18 vol. %), and magnetite (0–5 vol. %) occur in all run products except for three that crystallized at ≥1000°C and ≥300 MPa with an XH_2O_V of 1. Orthopyroxene formed in charges crystallized at 950°C and 100 MPa with an XH_2O_V of ≤0·8. Amphibole and olivine, however, were not detected in any of the crystallization run products.

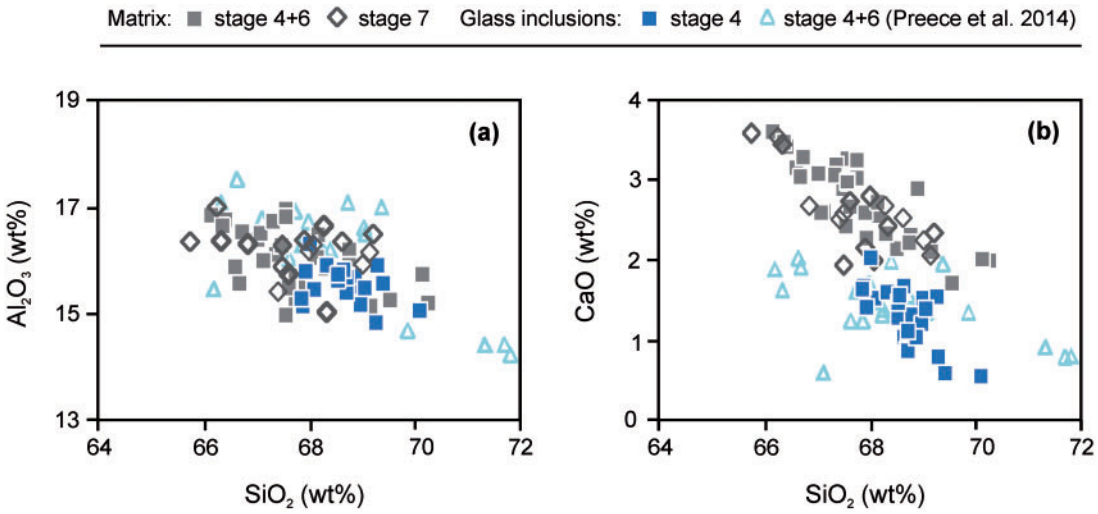

Fig. 6. Composition of matrix (glass plus microlites, analyzed with a 50 μm beam) and glass inclusions in clinopyroxene phenocrysts of stage 4 + 6 and stage 7 dome clasts. Data shown are from this study and from Preece *et al.* (2014).

The experimental glasses have a basaltic andesitic to dacitic composition (Fig. 7a). Those that have formed in charges crystallized at 950°C and ~200 MPa with an XH_2O_V of 0·7 and a melt H_2O content of ~3·6 wt % approach some of the least evolved matrix compositions of the natural samples with ~66 wt % SiO_2 and ~16·5 wt % Al_2O_3 (Fig. 7a). The experimental plagioclase compositions range from ~An50 to ~An90, compared with the overall more evolved rim compositions of the natural crystals with ~An40 to ~An90 (Fig. 7b). The plagioclase K_D (Ca–Na) values for crystal rims formed at 950°C and ~200 MPa (CE-7) increase from 3·6 to 5·9 with increasing melt H_2O and XH_2O_V of the charges (Supplementary Data Electronic Appendix A3). Clinopyroxene Wo and En contents of the experimental and natural crystals largely match (Fig. 7c), but the Al_2O_3 contents of the experimental crystals are high (>3–8 wt %) relative to the natural crystals (~1·2–7 wt %) (Fig. 7d and e). The clinopyroxene K_D (Fe–Mg) values for crystal rims formed at 950°C and ~200 MPa (CE-7) vary between 0·19 and 0·30, increasing with melt H_2O and XH_2O_V (Supplementary Data Electronic Appendix A3). The experimental and the natural magnetite crystals are comparable in their FeO and TiO_2 contents, whereas the Al_2O_3 contents of the experimental crystals are relatively high (Fig. 7f). We note that crystallization at variable oxygen fugacities (i.e. at strongly oxidizing, >NNO + 2 conditions in CE-1 compared with all other experiments run at ~NNO + 1·5 to NNO + 0·7) affects the TiO_2, FeO, and MgO contents of clinopyroxene, magnetite, and glass, but that it does not account for their high-Al contents (Fig. 7).

Run products of the melting experiments

The six melting experiments were performed in conjunction with the crystallization experiments at 925–1000°C, ~100–400 MPa, and at ~NNO + 1·5 to ~NNO + 0·7 (Table 3). Partial melting and partial crystallization of the basaltic andesite rock powders in charges with an XH_2O_V of ~0·4–1 resulted in run products with 0 to ~70 vol. % crystals (Table 3). Crystallinities of ~40–60 vol. %, which are characteristic for the natural samples, were obtained in charges recrystallized at ≤950°C with an XH_2O_V of ≥0·6 and in charges run at ≥975°C with an XH_2O_V of ≤0·7 (Table 3). Plagioclase (~7–66 vol. %), clinopyroxene (~0–18 vol. %), and magnetite (~0–5 vol. %) are present in all experimental products except for those of three charges run at 1000°C or ≥300 MPa and with an $XH_2O_V = 1$. Amphibole occurs in charges with an XH_2O_V of 1 and ~0·8 that were run at 925°C and ~200 MPa, forming clusters of randomly oriented crystals. Orthopyroxene is present in charges recrystallized at 950°C and ~100 MPa with an XH_2O_V ≤0·8, forming coarse dendritic crystals. The run products of the ≤950°C, ≤200 MPa melting experiments thus reproduce the mineral assemblage of natural samples from Merapi. Only olivine, which forms rare inclusions in natural amphibole phenocryts, was not detected.

The glasses of the melting experiments are basaltic andesitic to dacitic; those that formed in charges run at ≤950°C and ≤200 MPa with an XH_2O_V of ~0·5–0·6 match the moderately evolved natural matrix and glass inclusion compositions with ~68 and 16 wt % SiO_2 and Al_2O_3 (Fig. 8a). They have calculated H_2O and CO_2 contents of ≤3·3 wt % and ≥470 ppm, respectively (Table 3). Glass produced in charges of our ≥975°C and ≥300 MPa experiments, however, deviate from the natural matrix and glass compositions (Fig. 8a). Their SiO_2 and Al_2O_3 contents are <62 and >16·5 wt %, and their calculated melt H_2O contents are ≥3·8 wt %. Plagioclase crystal rims produced in the experiments have ~An40–85 composition, and thus compare with the range of rim compositions detected for the natural samples (Fig. 8b). Their average K_D (Ca–Na) values vary between 3·0 and 6·7 (Supplementary Data Electronic Appendix A3). The ~An50 composition, which is most common in the natural crystal rims, is reproduced in charges run at ≤200 MPa with an XH_2O_V of ~0·5–0·6 and a melt H_2O content of ≤3·3 wt % (Fig. 8b). Crystals with >An50 to ~An70 rims formed in charges with melt volatile and H_2O contents of ~3–5 wt % that were run at ≤200 MPa with an XH_2O_V of ≥0·8 or at ~400 MPa with an XH_2O_V of ~0·4. However, few cores and inner rims (≤5 vol. %) of newly crystallized plagioclase (<5–10 vol. %) in the low-pressure, ≤200 MPa experiments with a low XH_2O_V of ≤0·7 also have >An50 to ~An80 compositions, whereas their K_D (Ca–Na) values are significantly (>2σ) higher than those of the newly crystallized outer rims in the same charges.

Clinopyroxene rim compositions have ~En32–42, ~Wo40–50, ~1·8–8 wt % Al_2O_3, ~19–23 wt % CaO, and ~10–15 wt % MgO. Their K_D (Fe–Mg) values vary between 0·16 and 0·38, decreasing with increasing experimental temperature and increasing with experimental melt H_2O and XH_2O_V. Clinopyroxene with ~Wo42–43, ~En43, and ≤2 wt % Al_2O_3 that matches the most common natural rim compositions was approached in charges with an XH_2O_V of ≤0·6 and a melt H_2O content of ≤3·3 wt % at ≤200 MPa (Fig. 8c–e). Primitive natural clinopyroxene rim compositions, and in particular those with ≥46 Wo, ≥3 wt % Al_2O_3 and ≥22 wt % CaO, are produced at ≤200 MPa in charges with an XH_2O_V of ≥0·8 and at ≥300 MPa in charges with an XH_2O_V of ≤0·7 (Fig. 8b–d). Some cores and inner rims of newly crystallized clinopyroxene (<5–10 vol. %) in our ≤950°C, XH_2O_V ≤0·6 experiments, moreover, have high-Al_2O_3 (>2 to 6 wt %), low-CaO (<20 wt %) compositions that are unknown from the natural samples, but their modal proportion is low (<5–10 vol. %). Amphibole, which is a minor but characteristic constituent of Merapi basaltic andesites, formed in our melting experiments at 925°C and ~200 MPa, but was not detected in any of the higher temperature runs. Crystals from charges with an XH_2O_V of ~0·8 and a melt H_2O content of ~4·0 wt %

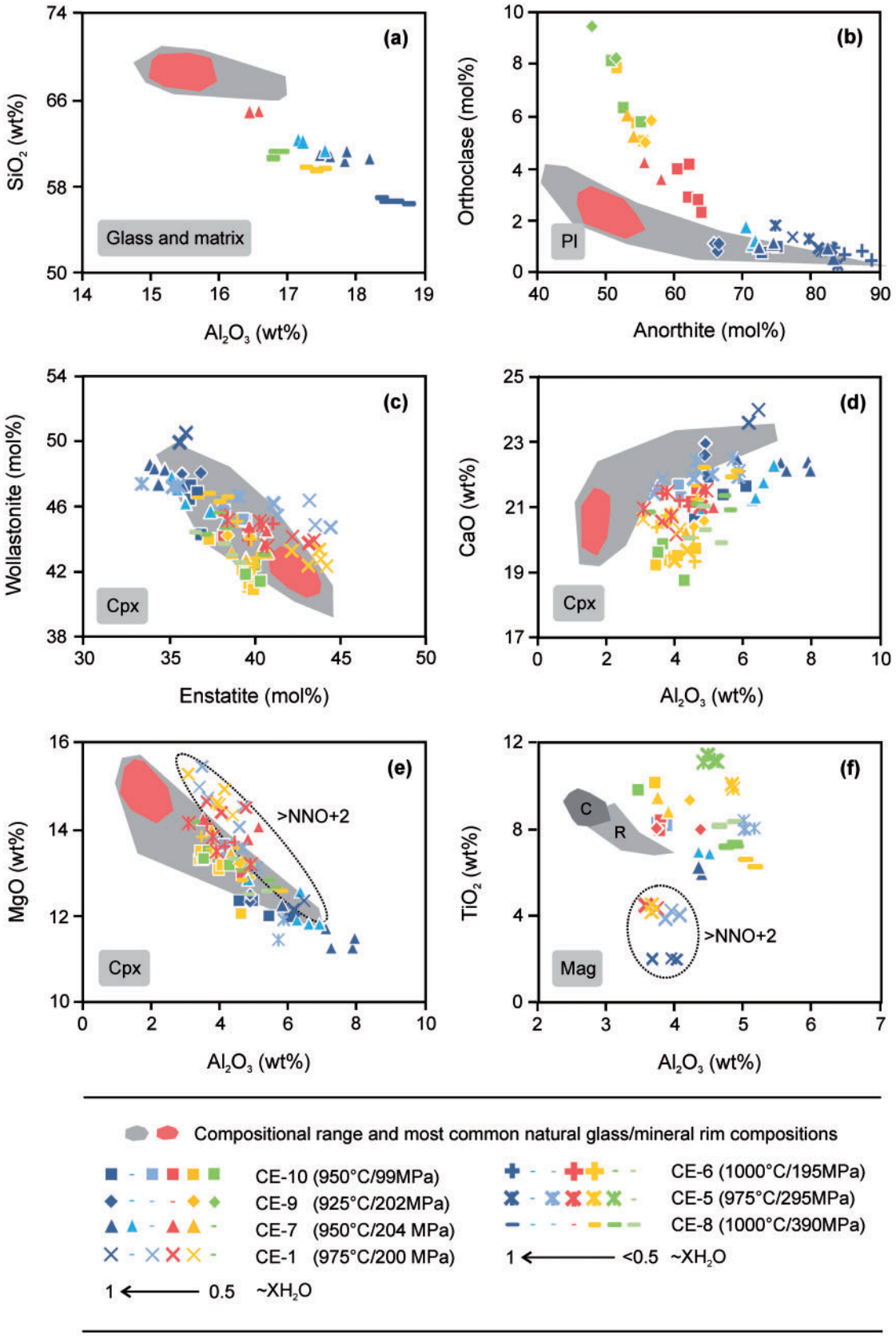

Fig. 7. Composition of the crystallization experiment (CE) run products compared with the natural phase assemblage: (a) glass compositions; (b–e) plagioclase and clinopyroxene rim compositions; (f) evolved magnetite core (C) and rim (R) compositions. The grey fields outline the range of the natural phase compositions; the red fields mark the most common compositions. All data are reported in Supplementary Data Electronic Appendices A2 and A3. Experiment CE-1 was performed at ~NNO >2·0; all other experiments were performed at ~NNO + 1·5 to ~NNO + 0·7.

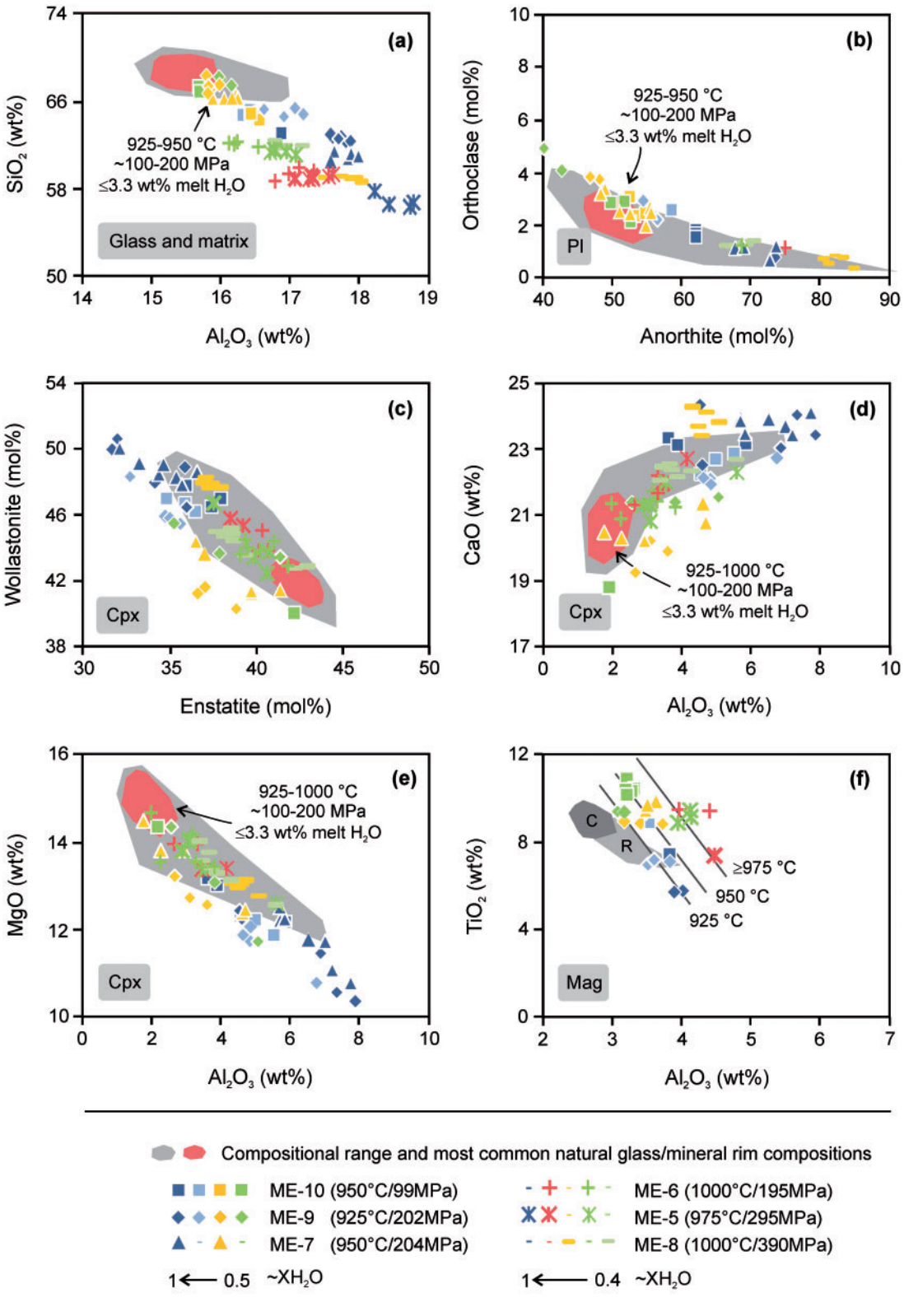

Fig. 8. Composition of the melting experiment (ME) glasses and newly crystallized outer mineral rims compared with the natural phase assemblage: (a) glass compositions; (b–e) plagioclase and clinopyroxene rim compositions; (f) evolved magnetite core (C) and rim (R) compositions. The grey fields mark the range of the natural phase compositions; the red fields show the most common compositions. (a) Glass and matrix, (b) plagioclase, (c–e) clinopyroxene, and (f) magnetite compositions. All data are reported in Supplementary Data Electronic Appendices A2 and A3. All experiments were performed at ~NNO + 1·5 to ~NNO + 0·7.

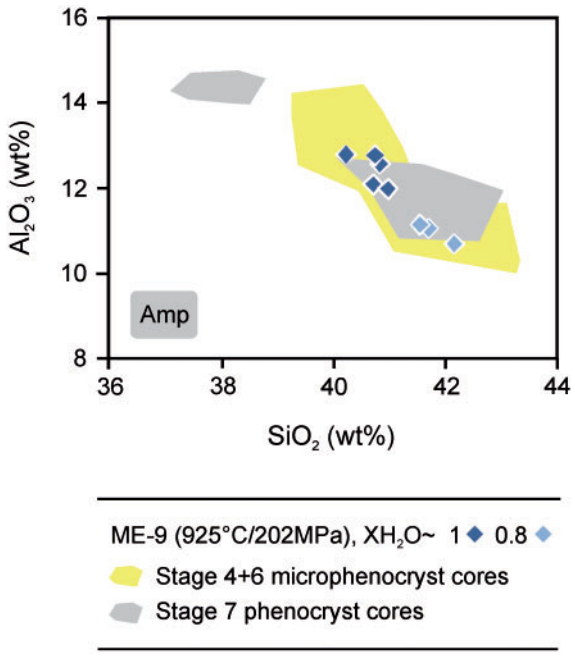

Fig. 9. Experimental and natural amphibole SiO_2 and Al_2O_3 core compositions. The experimentally produced amphibole compositions are closely comparable with those of the natural microphenocrysts, but they are significantly more evolved than the main amphibole phenocryst population with ~14 wt % Al_2O_3.

have compositions comparable with those of the Al-poor (~11 wt % Al_2O_3) natural microphenocryst cores (Fig. 9). Amphibole from charges with an $XH_2O_V = 1$ and a melt H_2O content of ~4·9 wt %, in contrast, approach the composition of the natural Al-rich (~13 wt % Al_2O_3) microphenocryst cores (Fig. 9). Magnetite compositions that approach those of the evolved natural crystals form at 925–950°C (Fig. 8f). The most evolved compositions, which are preserved in the natural crystal cores, were approached in charges with an XH_2O_V of ≤0·6, whereas the natural magnetite rim compositions are approached in charges with an XH_2O_V of ≥0·7 at 925 and 950°C (Fig. 8f). The natural ~En67 orthopyroxene compositions are reproduced at 950°C and ~100 MPa in charges with an XH_2O_V of ≤0·8.

DISCUSSION

We first evaluate the conditions of equilibrium in our crystallization and melting experiments and their potential for constraining the crystallization conditions in Merapi's pre-eruptive magma reservoir. We then compare the natural and the experimentally produced mineral assemblages and compositions (1) to constrain the crystallization conditions of the resident magma, (2) to characterize the components and conditions of the pre-eruptive magma recharge, and (3) to evaluate the processes that control the variation in crystallization conditions. We focus our discussion on interpreting the evolution of magmas involved in Merapi's 2010 eruption, but note that whole-rock compositions, mineral assemblages, and mineral and glass compositions are largely invariant in pyroclasts erupted between at least 1930 and 2010 (Berthommier, 1990; Abdurachman, 1998; Chadwick *et al.*, 2013; Costa *et al.*, 2013; Preece *et al.*, 2013). We therefore concur with previous studies that Merapi's shallow magma plumbing system has undergone no radical modifications in the last ~100 years, whereas variations in extensive parameters (e.g. volumes of resident and recharge magmas or the amounts of carbonate assimilation) may have been important (e.g. Borisova *et al.*, 2013; Costa *et al.*, 2013; Troll *et al.*, 2013).

Experimental constraints

Results from the crystallization experiments

The run products of our crystallization experiments show systematic modal and compositional variation as a function of experimental conditions (Fig. 10a and b; Table 3; Supplementary Data Electronic Appendix A3). Plagioclase anorthite content increases with increasing melt H_2O content and with experimental temperature (Fig. 10a). Average plagioclase K_D (Ca–Na) values also systematically increase with increasing melt H_2O content from 3·7 to 6·4 for melt H_2O contents of ~3·6–5·9 wt % (CE-7; Supplementary Data Electronic Appendix A3), and they are comparable with values determined by previous studies for compositionally comparable systems (e.g. Sisson & Grove, 1993; Pichavant *et al.*, 2002; Parman *et al.*, 2011). Clinopyroxene CaO content also increases with melt H_2O content, but decreases with increasing pressure, whereas it shows little variation as a function of experimental temperature (Fig. 10b). Average clinopyroxene K_D (Fe–Mg) values of between 0·20 and 0·30 decrease with temperature and increase with increasing melt H_2O content (Supplementary Data Electronic Appendix A3), and they also are comparable with values determined in other studies (e.g. Sisson & Grove, 1993; Pichavant *et al.*, 2002; Parman *et al.*, 2011). We suggest that both the systematic compositional variation of the crystallization experiment run products and partition coefficients that are comparable with literature values indicate a close approach to equilibrium in our experiments as intended (see Table 2). That the run products failed to reproduce the natural mineral and glass compositions could indicate that the temperature, pressure, XH_2O, or fO_2 conditions did not match those of the natural system or that our starting material represents a non-liquid composition. We rule out the interpretation that the explored temperature, pressure, and XH_2O conditions are inadequate, because the crystallinities characteristic for the natural samples and the melt H_2O contents were well reproduced. We also rule out the interpretation that the moderately oxidizing crystallization conditions (at an fO_2 of ~NNO + 1·5 to ~NNO + 0·7) are the cause of the compositional mismatch between the crystallization experiment run products and the natural samples, because the Fe–Mg–Ti compositions of the experimental and the natural clinopyroxene, magnetite, and glasses are well matched. The unmatched high Al

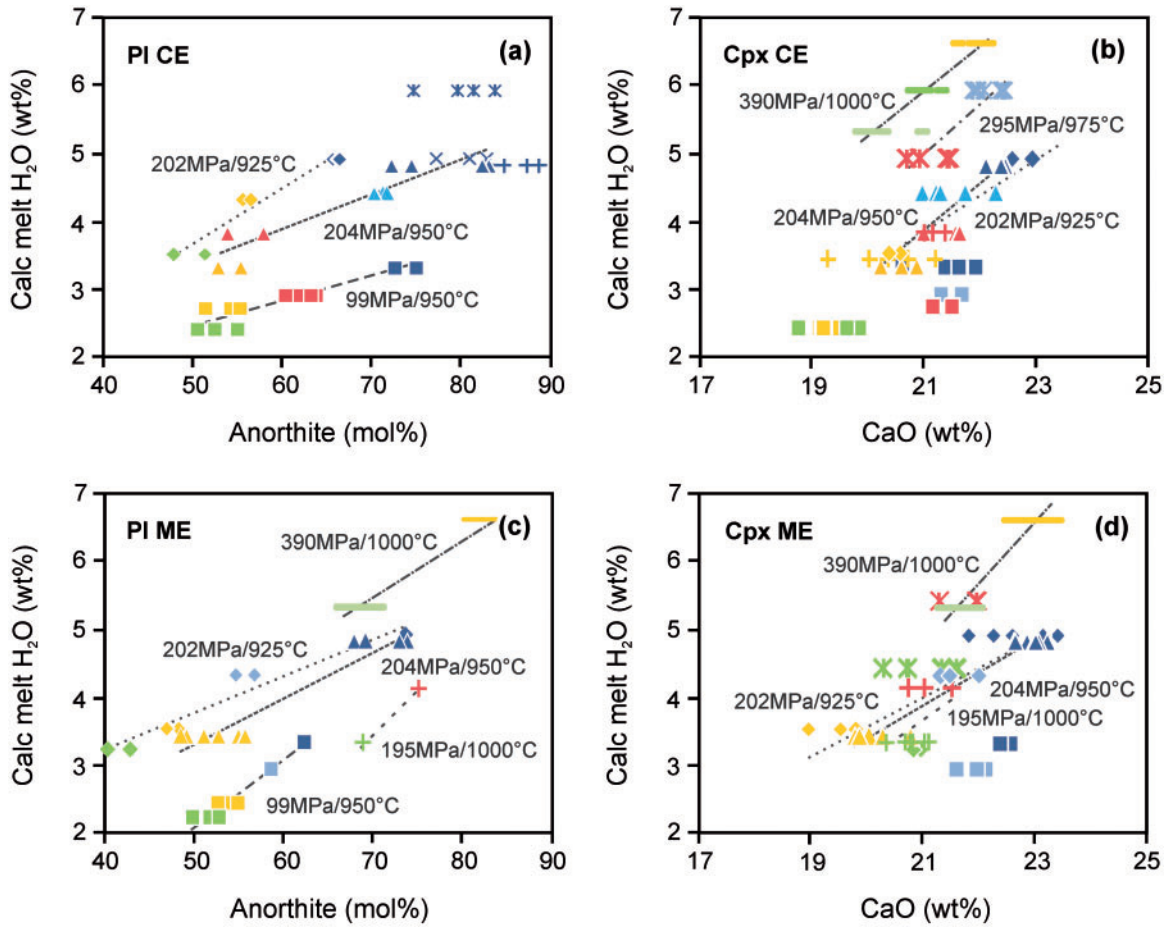

Fig. 10. Systematic compositional variation of plagioclase and clinopyroxene as a function of experimental conditions in the crystallization experiments (a, b; mineral core compositions) and melting experiments (c, d; outer mineral rim compositions). Symbols in (a) and (b) correspond to those of Fig. 7, and those in (c) and (d) correspond to those in Fig. 8. Compositional trends are indicated for charges with variable XH_2O_V and melt H_2O contents crystallized at the indicated pressure and temperature conditions. That the run product compositions of the melting experiments are more weakly correlated than those of the crystallization experiments reflects our use of rock powder as a starting material, which introduced some compositional variation between and within the charges. Calc melt H_2O is melt H_2O content calculated using VolatileCalc of Newman & Lowenstern (2002).

contents of minerals and glasses, in contrast, are not affected by variations in fO_2 (Fig. 7). We therefore suggest that our starting material represents a non-liquid composition; that is, we infer that the sample from which we fused our starting glass comprises accumulated cognate, antecrystic and xenocrystic components and mixed liquids, which is consistent with Merapi's inferred open-system evolution (e.g. Chadwick *et al.*, 2007, 2013; Nadeau *et al.*, 2011, 2013; Borisova *et al.*, 2013; Costa *et al.*, 2013; Van der Zwan *et al.*, 2013; Erdmann *et al.*, 2014). As a result, we cannot use the phase proportions or compositions from our crystallization experiments to constrain the conditions in Merapi's pre-eruptive magma reservoir; instead, we use their compositions below to interpret the mineral rim compositional variation detected in our melting experiments.

Results from the melting experiments

Compared with the crystallization experiments, melting experiments of the type performed have the advantage that they partially preserve the original crystal assemblage that was present in the magmas stored within the pre-eruptive reservoir, including xenocrysts, antecrysts, and accumulated or mixed phenocryst populations. The experimental conditions closely match the crystallization conditions in the pre-eruptive reservoir if (1) all microlites that crystallized during magma ascent have melted and (2) all phenocrysts in the charges and their rim compositions match those of the natural samples. Melting experiments are thus suitable for characterizing the late-stage crystallization conditions in Merapi's crystal-rich pre-eruptive reservoir; however, it has to be kept in mind (and is considered further below) that the matrix of the starting rock powders may nevertheless contain components of the resident and the recharge melts. As in the crystallization experiments, the outer mineral rim and glass compositions produced in our melting experiments show systematic modal and compositional variations as a function of experimental conditions and partition coefficients comparable with those determined by previous studies (e.g. Sisson & Grove,

1993; Pichavant *et al.*, 2002; Parman *et al.*, 2011). Plagioclase anorthite content (Fig. 10c) and average K_D (Ca–Na) values (3·0–6·7) increase with increasing melt H_2O content, XH_2O_V, and with experimental temperature (Supplementary Data Electronic Appendix A3). The detected compositional variation of the outer plagioclase rims in single charges is nearly always within ± 2–3% (rarely within ± 4%) of the average SiO_2 and Al_2O_3 contents, indicating that local equilibrium was approached throughout the charges. Clinopyroxene CaO contents increase with melt H_2O content and XH_2O_V (Fig. 10d), whereas average K_D (Fe–Mg) values (0·15–0·38) decrease with increasing experimental temperature and increase with melt H_2O content and XH_2O_V (Supplementary Data Electronic Appendix A3). The detected compositional variation of the outer clinopyroxene rims in single charges varies within up to ± 5% of the average SiO_2 and CaO contents (whereas minor components such as Al_2O_3 have a variance of up to 50%). The major element compositional variation of clinopyroxene outer rims within single charges is larger than that of the outer plagioclase rims, but nevertheless is relatively homogeneous within charges. However, some of the cores and inner rims of newly crystallized plagioclase and clinopyroxene in low-pressure (≤200 MPa), low-XH_2O_V (≤0·7) experiments clearly record partial disequilibrium. The >An50 to ~An80 compositions and disequilibrium K_D values of inner zones of new plagioclase, and equilibrium K_D (Fe–Mg) values, but high-Al_2O_3 (>2 to 6 wt %), low-CaO (<20 wt %) compositions of inner zones of new clinopyroxene, differ by >2σ from the compositions of outer crystal rims (which is unknown from the natural samples). They are interpreted to record early stages of experimental crystallization probably during heating and at high fluid/melt ratios, and they are therefore not considered in the subsequent discussion. Their effect on the composition of the reactive system is nevertheless considered to be limited, given that they have a low proportion of <5–10 vol. % of all newly crystallized plagioclase and clinopyroxene. That the mineral rim and glass compositions of the melting experiments nevertheless follow compositional trends that are comparable with those of the crystallization experiments (Fig. 10c and d versus Fig. 10a and b), that plagioclase–melt and clinopyroxene–melt partition coefficients are comparable with equilibrium values, and that outer rim compositions within single charges have relatively homogeneous compositions (Supplementary Data Electronic Appendix A3) is taken as evidence that the experiments approached local equilibrium conditions as intended.

In the following sections, we therefore use the mineral rim and glass compositions produced in the melting experiments to infer the crystallization conditions of the resident magma in Merapi's pre-eruptive reservoir, and to approximate the conditions of the pre-eruptive recharge. We also compare the crystallinities between the natural and the experimental samples, but not their mineral proportions, because we cannot accurately determine the volume of, for example, co-crystallizing plagioclase and clinopyroxene in the natural basaltic andesites (this would require extensive compositional mapping). We suggest that the conditions of the resident magma can be closely constrained by this approach, because the compositionally primitive mineral zones (and microlites) that crystallized from the recharge magma remain unmelted. We further suggest that the compositional variation detected in our melting experiments can be used to closely approximate the recharge crystallization conditions in Merapi's pre-eruptive reservoir, because the compositional difference between the resident melt (inferred to correspond to the evolved matrix and glass inclusion compositions with ~68 wt % SiO_2 and ~15·5 wt % Al_2O_3; Fig. 6a) and the recharge melt (inferred to approach the primitive matrix and glass inclusion compositions with ≤66 wt % SiO_2 and ≥17 wt % Al_2O_3; Fig. 6a) is limited and the effect on our estimate is thus minor. Previous crystallization experiments with basaltic and basaltic andesitic starting materials with a compositional difference of ≤3 wt % SiO_2 and ≤1 wt % Al_2O_3 but otherwise identical crystallization conditions, for example, yielded equivalent plagioclase and clinopyroxene compositions in charges in which both minerals co-crystallized [e.g. 79-35 g # 12 and 82-66 #5 of Sisson & Grove (1992) or SAR3 and SAR16 of Parman *et al.* (2011)]. We therefore infer that the results of our melting experiments can be used for estimating both the intensive parameters of the resident magma and those of the recharge magma. We acknowledge that estimating the crystallization conditions on the basis of our melting experiments is more uncertain than for estimates based on crystallization experiments (owing to our use of a starting rock powder that introduced some compositional variation between charges), but that uncertainties are lower than the increments at which we have varied the intensive parameters (i.e. up to ± 25°C and ± 75 MPa). Uncertainties in the calculated melt H_2O contents (Table 3) are ± 1 wt %, whereas those of the calculated melt CO_2 contents (Table 3) are large, up to ± 1000 ppm (see Baker & Alletti, 2012). Fluctuations of H_2O and CO_2 in Merapi's pre-eruptive reservoir, however, are inferred on the basis of mineral compositional variations, and not on the basis of the calculated CO_2 values.

Shallow, H_2O-poor pre-eruptive magma storage

Consistent with previous studies, we suggest that the pre-eruptive magma storage conditions in Merapi are recorded by the compositionally evolved mineral zones and by the evolved matrix (glass plus microlites) and glass inclusion compositions in the erupted, crystal-rich basaltic andesites (Table 4; see also Costa *et al.*, 2013; Nadeau *et al.*, 2013; Erdmann *et al.*, 2014). Crystallinities of >40 to ~60 vol. % and the predominant, ~An50 natural plagioclase and Al-poor clinopyroxene compositions are simultaneously reproduced in our melting experiments performed at 925–950°C, ~100–200 MPa,

Table 4: Components and inferred crystallization conditions for Merapi's magma plumbing system

Reservoir:	Pre-eruptive (main)	Pre-eruptive (shallow)	Pre-eruptive	Deep, unconstrained
Magma:	Resident	Resident	Recharge	Recharge
Components				
Pl	~An50	~An40	≤An70	~An90
Cpx	~Wo42–43	≤Wo42	≤Wo50	~Wo48
Amp	~11 wt % Al_2O_3	—	~13 wt % Al_2O_3	~14 wt % Al_2O_3
Mag	~3 wt % Al_2O_3	~3 wt % Al_2O_3	≥3·5 wt % Al_2O_3	~6 wt % Al_2O_3
Opx	—	~En67	—	—
Ol	—	—	—	>Fo60–70
Melt	~68–69 wt % SiO_2	~69–70 wt % SiO_2	~66 wt % SiO_2	?
Conditions				
Melt H_2O content	~3–4 wt %	~3 wt %	~4–5 wt %	?
XH_2O_V	~0·5–0·6 ± 0·1	~0·5–0·6 ± 0·1	~0·8	?
Temperature	~925 to 950 ± 25°C	~925 to 950 ± 25°C	>950 to <1000°C	?
Pressure	~200 ± 75 MPa	≥100 MPa	~200 ± 75 MPa	?

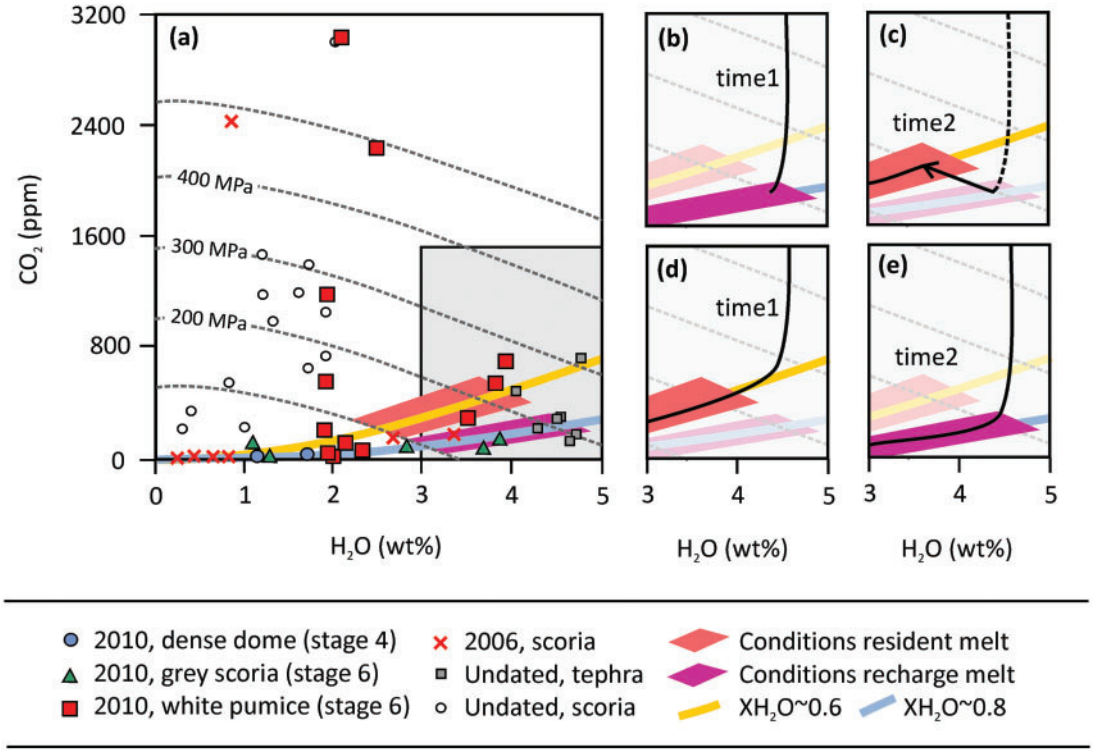

Fig. 11. Glass inclusion compositions, estimated resident and recharge melt H_2O–CO_2 contents, and inferred volatile evolution. (a) Glass inclusion compositions from Nadeau *et al.* (2013) and Preece *et al.* (2014); redrawn from Preece *et al.* (2014) with our estimates for resident and recharge melt compositions and vapour isopleths at an XH_2O_V of ~0·6 and ~0·8. (b–d) Insets shown in (a). (b, c) Scenario 1: Merapi's pre-eruptive reservoir is filled by magmas with an XH_2O_V of ~0·8 (b, time 1) that become relatively H_2O-poor as a result of CO_2-rich volatile fluxing during magma storage (c, time 2). (d, e) Scenario 2: the reservoir is filled by magmas with an XH_2O_V of ~0·6 during inter-eruptive periods (c, time 1) and by magmas with an XH_2O_V of ~0·8 during pre-eruptive periods (d, time 2). We favour the interpretation of Scenario 2, proposing that magmas ascending during inter-eruptive periods (at time 1) approach a vapour-buffered degassing path, whereas magmas ascending during pre-eruptive periods (at time 2) approach a closed-system degassing path.

with an XH_2O_V of ~0·5–0·6, and at a melt H_2O content of <3·3 wt % (Table 3; Fig. 8b, d and e). The evolved matrix and glass compositions of the natural samples with ~68–69 wt % SiO_2 and ~15·5 wt % Al_2O_3 are also closely approached at these experimental conditions (Fig. 8a). Their calculated melt H_2O and CO_2 contents of ≤3·3 wt % and ~240–590 ppm, moreover, match the volatile contents of some of the natural glass inclusions analyzed by Preece *et al.* (2014) (Fig. 11). Amphibole with compositions approaching those of the evolved microphenocrysts of our stage 4 + 6 samples formed in charges run at 925°C with an XH_2O_V of ~0·8 and an estimated melt H_2O content of ~4·0 wt %, but not at 950°C. Magnetite comparable with the evolved core composition of the natural samples also formed in charges run at 925°C (Fig. 8f). In combination, the mineral and glass compositions and crystallinities indicate that Merapi's pre-eruptive reservoir crystallizes at predominantly ≤200 MPa, at a temperature of ~950°C and ≥925°C, and with a melt H_2O content of ~3–4 wt % (Table 4; Fig. 12a

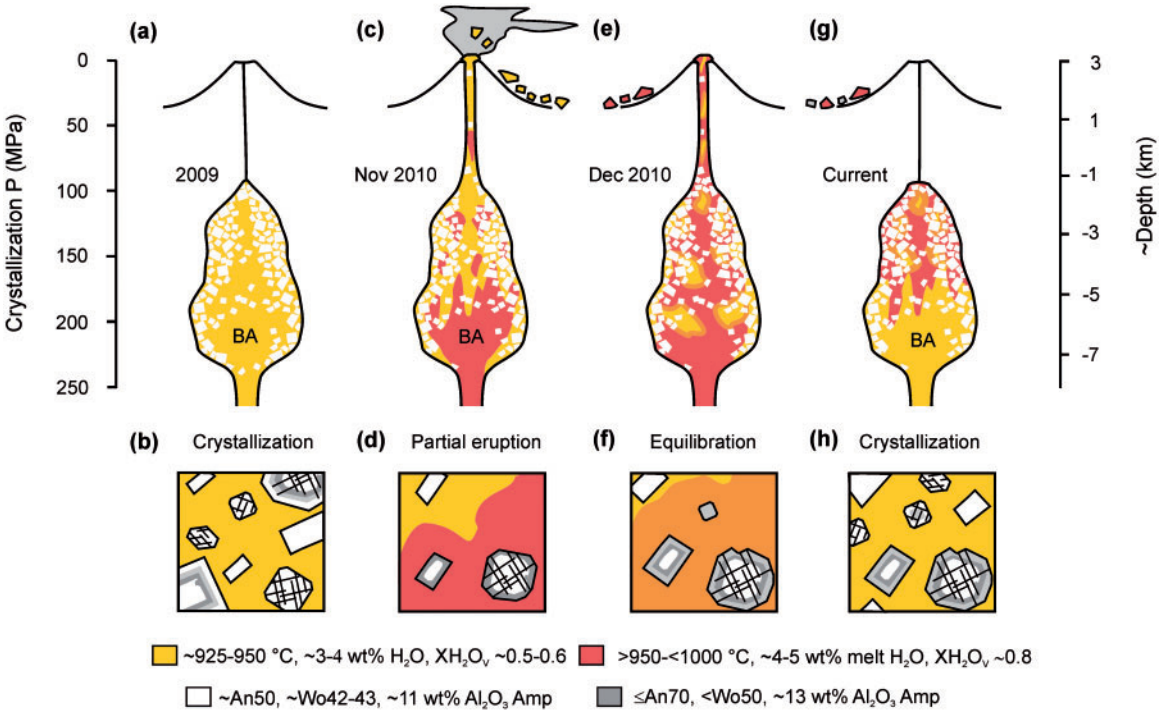

Fig. 12. Sketch summarizing the estimated crystallization conditions for Merapi's pre-eruptive magma storage reservoir, its location and the main processes proposed for its evolution prior to recent historical eruptions, showing a timeline leading up to the 2010 eruption. (a, b) During inter-eruptive storage, Merapi's basaltic andesitic magmas crystallize an evolved mineral assemblage. (c, d) During pre-eruptive magma recharge, the reservoir is replenished by magma with an H_2O-rich melt and vapour phase, crystallizing mineral zones of intermediate composition. (e, f) The intensive parameters of magma parcels of the original resident and the recharge magma equilibrate. (g, h) Inter-eruptive recharge by magma with an H_2O-poor melt and vapour phase begins. The inferred time scales of this evolution need to be assessed by detailed mineral composition diffusion modelling. We further note that the geometry of the magma storage zone is unconstrained by our data, except that we infer that the erupted magma and its phenocrysts must have collected over a pressure range of ~100 MPa, equivalent to a depth range of ~4·5 km. BA = basaltic andesite.

and b). Experimental orthopyroxene of composition ~En68, which closely corresponds to the natural ~En67 crystal compositions, crystallized at 950°C and ~100 MPa in equilibrium with an XH_2O_V of ~0·6 and a melt H_2O content of ~2·4 wt %, further indicating that Merapi's pre-eruptive reservoir extends to levels shallower than a depth equivalent to 200 MPa (Tables 3 and 4; Fig. 12). Consistent with the experimental assemblage, we further propose that the natural plagioclase crystals with compositions of ~An40–50 and clinopyroxene crystals with ≤Wo42 and ≤19·5 wt % CaO have formed in this shallow reservoir region, in agreement with the interpretations of Costa *et al.* (2013). The melt H_2O and CO_2 contents of ~2·4 wt % and ~240 ppm calculated for these conditions also match those detected in several natural glass inclusions (see Preece *et al.*, 2014). That the Fe, Mg, and Ti contents of glass, clinopyroxene, orthopyroxene, and magnetite produced in charges run at an fO_2 of ~NNO + 1·0 and an XH_2O_V of ≤0·6 replicate the natural mineral and glass compositions indicates moderately oxidizing crystallization conditions (Table 3).

We emphasize that the evolved mineral and glass inclusion compositions characteristic of Merapi basaltic andesites were in equilibrium and that they all record crystallization in the pre-eruptive reservoir. Previous studies, in contrast, have suggested that crystals and glass inclusions record magma evolution at deep and shallow levels, respectively, and thus that their record of crystallization conditions is largely decoupled (Nadeau *et al.*, 2013; Preece *et al.*, 2014). Our estimated magma storage temperature of ≥925–950 ± 25°C is consistent with the crystallization temperatures calculated using evolved amphibole compositions and the Ridolfi *et al.* (2010) or the Ridolfi & Renzulli (2012) calibrations (i.e. ~920–970 ± 50°C; Costa *et al.*, 2013; Nadeau *et al.*, 2013; Erdmann *et al.*, 2014). Calculated clinopyroxene crystallization temperatures of ~1025 to 1060 ± 59°C (Preece *et al.*, 2014) using the thermometer of Putirka *et al.* (2003) are comparatively high, but the lower estimated crystallization temperatures are within the error of our estimate. The inferred shallow pre-eruptive storage at ≥100–200 ± 75 MPa indicates that Merapi's pre-eruptive reservoir is located at a depth of ≥4·5 to ~9 ± 3 km, and thus within the carbonate-dominated upper crust (see Smyth *et al.*, 2005), if we assume an average overlying crustal density of 2242 kg m^{-3} (see Tiede *et al.*, 2005) and lithostatic pressure conditions. If the reservoir was under significant overpressure (see Costa *et al.*, 2013; Genareau *et al.*, 2014), then we infer

that it is located at even shallower levels (e.g. at ≥2·5 to 7 ± 3 km for an overpressure of ≤50 MPa). A shallow, ephemeral magma storage zone at ~1·5–2·5 km below Merapi's summit, which has been proposed (Ratdomopurbo & Poupinet, 1995, 2000; Saepuloh *et al.*, 2010; Nadeau *et al.*, 2013) but also contested on the basis of geophysical data and petrological data (Beauducel & Cornet, 1999; Müller & Haak, 2004; Costa *et al.*, 2013), is not evident from our results. Our pressure estimates, however, are consistent with seismic and ground deformation data, which suggest magma storage at depths of ≥5·5 to ~8·5 km below Merapi's summit, from at least 1992 to 2010 (Ratdomopurbo & Poupinet, 1995, 2000; Beauducel & Cornet, 1999; Budi-Santoso *et al.*, 2013). Our results are also consistent with glass inclusion barometry, which has been used to infer re-equilibration of magmas at ≤265 MPa and depths of ≤10 km (Preece *et al.*, 2014), but they differ significantly from previous estimates based on amphibole and clinopyroxene barometry, which have suggested a main zone of pre-eruptive magma storage at >100–400 or at ~400–500 MPa (Gertisser, 2001; Chadwick *et al.*, 2013; Costa *et al.*, 2013; Preece *et al.*, 2014). This result is not surprising, considering the uncertainties of the barometric methods employed (e.g. Fig. 1; Nimis, 1999; Putirka, 2008; Erdmann *et al.*, 2014). Crystallization pressure calculated for clinopyroxene using the Nimis (1999) barometer, which is not recommended for calc-alkaline compositions, yields moderate to high calculated pressures of ~400–500 MPa for Merapi's main clinopyroxene crystal population if the crystallization temperature is moderately overestimated [i.e. at 1000°C in estimates of Chadwick *et al.* (2013)], and lower calculated pressures of ~200–400 MPa if the crystallization temperature is largely overestimated [i.e. at 1050°C in estimates of Preece *et al.* (2014)]. For clinopyroxene that crystallized from more evolved magmas than the Merapi basaltic andesites, even higher pressure overestimates would result (Fig. 1a). That a large range in crystallization pressure is calculated with the Nimis (1999) calibration (e.g. Chadwick *et al.*, 2013) is inevitable if the natural clinopyroxene crystals formed over a range of temperatures, but average clinopyroxene crystallization temperatures are assumed (e.g. over- and underestimates of crystallization temperatures by 20°C propagate into a 100 MPa decrease or increase in the calculated pressure; Nimis, 1999). The clinopyroxene crystallization pressure calculated for Merapi's magma system using the geobarometer equations (32b) and (32 c) of Putirka (2008) yields pressure estimates of predominantly ~200–300 and ~100–200 MPa (Preece *et al.*, 2014). These agree well with our estimate, reflecting the fact that the barometers yield values that approach known crystallization pressures for clinopyroxene crystallized from mafic–intermediate magmas at moderately low temperatures (Fig. 1b and c). We point out, however, that the values calculated for Merapi are (1) based on largely overestimated clinopyroxene crystallization temperatures of 1025–1058°C, which increases the calculated pressure values, and (2) based on estimated primitive melt composition that corresponds to Merapi basaltic andesite whole-rock compositions (instead of dacitic compositions as recorded by glass inclusions), which decreases the calculated pressure values. The pressure estimates for the Merapi system based on the amphibole barometers of Ridolfi *et al.* (2010) and Ridolfi & Renzulli (2012) yield minimum values of ~250–400 MPa, reflecting that the method calculates intermediate pressures for amphibole crystallized in equilibrium with dacitic melts (Fig. 1d; Erdmann *et al.*, 2014).

We emphasize that using single mineral thermometers or barometers to estimate the crystallization conditions of mixed magma systems has no advantage over experimental constraints, because any compositional variations in the magma and melt that complicate the experimental estimates equally affect the thermobarometric estimates. It is, moreover, important to keep in mind that errors on the calculated conditions may significantly exceed the standard errors of the methods, if the employed mineral thermometers or barometers were calibrated based on compositions or intensive parameters (e.g. P, T, fO_2, or XH_2O) unlike those of the investigated system.

The geometry of Merapi's shallow magma system cannot be constrained on the basis of our results or previous barometric estimates, but we emphasize that the erupted magma and its phenocryst cargo was assembled over a significant pressure and depth range of ~100 MPa and ~4·5 km. The pre-eruptive magma reservoir outlined in Fig. 12 highlights this depth range, but we cannot resolve if the magma storage zone is a single reservoir or a number of shallow sub-reservoirs connected by dykes as proposed by Chadwick *et al.* (2013) and Nadeau *et al.* (2013). An elliptical, subhorizontal magma source at a depth of ~8·5 km was predicted for the 1996–1997 eruption on the basis of global positioning system (GPS) deformation and tilt data (Beauducel & Cornet, 1999); this is more consistent with a plumbing system consisting of several sub-reservoirs, but remains to be confirmed. In the future, currently installed continuous GPS and tiltmeters (CVGHM/BPPTK and DOMERAPI projects) will provide tighter constraints.

Pre-eruptive, H_2O-rich magma recharge

The recharge of Merapi's magma storage reservoir by a larger than average volume of volatile-rich mafic magma has been suggested in several previous studies to have played a key role in triggering and driving its paroxysmal 2010 eruption (e.g. Budi-Santoso *et al.*, 2013; Costa *et al.*, 2013; Jousset *et al.*, 2013; Preece *et al.*, 2013, 2014). Petrological studies have considered phenocrysts with primitive compositions and An-rich microlites as evidence for this recharge, but have

pointed out that the juvenile materials erupted in 2010 all have a homogeneous basaltic andesite composition (Costa *et al.*, 2013; Preece *et al.*, 2014; Fig. 2). More important is that the stage 7 samples, which have a higher proportion of pristine phenocrysts with primitive core and rim compositions that record the pre-eruptive recharge (Figs 3 and 4), also are closely comparable in composition with the stage 4 + 6 samples. We therefore suggest that the recharge magma of the 2010 event was basaltic andesitic and close in composition to the resident magma, at least in terms of major elements. This is important, because it indicates that magmas crystallize to a crystal-rich mush and mix in Merapi's shallow pre-eruptive reservoir, but that they do not significantly fractionate at this level. If any significant differentiation takes place, it must be at deeper levels of the magma plumbing system.

The most direct evidence for magma recharge and mixing within Merapi's pre-eruptive reservoir is the assemblage of normally zoned plagioclase, clinopyroxene, amphibole and magnetite phenocrysts with primitive core compositions [i.e. ~An90, ~Wo48, ~14 wt % Al_2O_3 amphibole, and ~6 wt % Al_2O_3 magnetite; Table 4; see also Costa *et al.* (2013) and Nadeau *et al.* (2013)]. The evolved ~Fo60–70 composition, low NiO (<0·25 wt %) and high CaO (>0·1 wt %) and MnO (>1 wt %) contents of rare olivine inclusions are characteristic for crystallization from basaltic andesitic magmas at <1000°C (e.g. Sisson & Grove, 1992; Moore & Carmichael, 1998), and we thus interpret them as recorders of magma evolution in Merapi's magma storage system and not as mantle-derived xenocrysts. We further consider the Al-poor (~12 wt % Al_2O_3) amphibole phenocrysts of the stage 7 samples as part of the primitive recharge assemblage, suggesting that they crystallized by replacing early stage olivine phenocrysts; this explains their common olivine inclusions, patchy zoning, and their high SiO_2/Al_2O_3 contents as compared with the predominant population of Al-rich amphibole phenocrysts. Similar textures have been reported, for example, from andesites formed by mixing of evolved and primitive magmas (Foley *et al.*, 2013; Kiss *et al.*, 2014). The characteristic ~An90 plagioclase and ~Wo48 clinopyroxene core compositions of Merapi's phenocrysts are reproduced in our H_2O-rich charges crystallized at 400 MPa and 1000°C, whereas amphibole, magnetite, or olivine that are part of the recharge assemblage did not form in the experiments. Whether this indicates that they crystallized from a magma that differed in composition from our starting material (e.g. from a basaltic magma or from one that was uncontaminated by calc-silicate components), or whether they crystallized at pressure and temperature conditions that were not explored by us (e.g. at >400 MPa or at ≤400 MPa and <1000°C) needs to be established in future studies. The low proportion (≤15 % of all phenocrysts) of the primitive, normally zoned recharge phenocrysts in Merapi's basaltic andesites is notable, but is comparable with the proportion of recharge phenocrysts observed in other compositionally homogeneous, crystal-rich magmas such as those that have erupted in recent decades at Mount St Helens (Berlo *et al.*, 2007; Streck *et al.*, 2008; Cashman & Blundy, 2013).

We consider it possible that some of the An-rich plagioclase and Ca-rich clinopyroxene crystals in the Merapi magmas may be derived from the disaggregation or the assimilation of calc-silicate xenoliths, as has been inferred on the basis of plagioclase $^{87}Sr/^{86}Sr$ compositions (Chadwick *et al.*, 2007), plagioclase and pyroxene $\delta^{18}O$ compositions (Troll *et al.*, 2013), calcic glass inclusions in some phenocrysts (Borisova *et al.*, 2013; see also Deegan *et al.*, 2010), and whole-rock trace element, $^{87}Sr/^{86}Sr$, and $\delta^{18}O$ compositions (Chadwick *et al.*, 2007; Borisova *et al.*, 2013; Troll *et al.*, 2013). We note, however, that calc-silicate xenoliths are rare in the Merapi basaltic andesites erupted in 2010 (≪1 vol. %) and that clinopyroxene approaching wollastonite in composition has not been detected in any significant proportion (Borisova *et al.*, 2013; Costa *et al.*, 2013; Preece *et al.*, 2014; our data), whereas it forms one of the main constituents of locally occurring calc-silicate xenoliths (e.g. Chadwick *et al.*, 2007; Troll *et al.*, 2013; our unpublished data). More important is that Merapi's basaltic andesites have 'typical' CaO contents (e.g. <10 wt % at ~52 wt % SiO_2; Fig. 2d) compared with those of other calc-alkaline basaltic andesites (e.g. Ambrym, Picard *et al.*, 1994; Soufrière Hills, Murphy *et al.*, 2000; Tatara San Pedro volcanic complex, Dungan *et al.*, 2001; Mont Pelée, Pichavant *et al.*, 2002). Small amounts (<2 wt %) of carbonate assimilation, as inferred by Chadwick *et al.* (2007), are consistent with the CaO contents and other compositional and mineralogical features of the Merapi magmas. Large amounts of inferred carbonate assimilation of up to ~20 or 15–40 wt % (see Borisova *et al.*, 2013; Troll *et al.*, 2013) should, however, clearly result in strongly CaO-enriched whole-rock compositions, as Costa *et al.* (2013) have previously shown.

Volumetrically more abundant than the primitive phenocrysts are intermediate zones and rims on phenocrysts of the resident magma and rims on the recharge magma phenocrysts with >An50 to ~An70 and >Wo43 to ~Wo50 composition, and amphibole microphenocrysts with ~13 wt % Al_2O_3 cores (Fig. 6). We infer that they crystallized in equilibrium with a melt that was close in composition to the least evolved matrix and glass inclusions in Merapi basaltic andesites with <67 and probably ≥65 wt % SiO_2 (Fig. 7a). We rebut the interpretation that the intermediate plagioclase and clinopyroxene compositions and the Al-rich amphibole microphenocrysts represent crystallization at elevated pressures, involving large-scale convection and downcycling, because this process is unlikely to produce the following features: (1) the commonly observed sawtooth-like zoning patterns in plagioclase and the characteristic compositional plateau zones of plagioclase and clinopyroxene; (2) the texturally and compositionally

bimodal amphibole population; (3) the mineral rims with intermediate compositions (they should have developed evolved overgrowths during their return flow to shallower levels of the reservoir). The crystallization of the ≤An70 plagioclase, ≤Wo50 clinopyroxene, and amphibole microphenocrysts with ~13 wt % Al_2O_3 may thus record crystallization in the pre-eruptive reservoir following magma recharge at an elevated temperature and/or at an elevated melt H_2O content.

Plagioclase with a characteristic ~An70 composition, which matches the compositions common in intermediate zones and rims of the natural crystals, is produced in our melting experiments at 1000°C, and at the same 200 MPa pressure, XH_2O_V of ~0·5–0·6, and a melt H_2O content of ~3–4 wt % that we infer for the pre-eruptive crystallization conditions of the resident magma (Table 3; Fig. 8b). Magnetite with ≥3·5 wt % Al_2O_3, which matches the rim composition of the natural crystals, also forms at these conditions (Fig. 8f). However, the Wo and Al_2O_3-rich compositions of clinopyroxene or amphibole that are characteristic of the recharge magma do not crystallize at these conditions (Fig. 8c and d). That the ~An70 plagioclase and ≤Wo50 clinopyroxene, Al-rich amphibole microphenocrysts, and Al-rich magnetite rims record magma recharge with an increase in temperature alone therefore seems unlikely. In contrast, the assemblage with ~An70 plagioclase, clinopyroxene with ≤Wo50 and ≥4 wt % Al_2O_3, amphibole with ~13 wt % Al_2O_3, and magnetite with ≥3·5 wt % Al_2O_3 is produced in our melting experiments at 925–950°C, ~200 MPa, an XH_2O_V of ≥0·8, and with a melt H_2O content of ~4–5 wt % (Fig. 8b–f). The most primitive natural matrix and glass inclusion compositions with ~66 wt % SiO_2 and ~17 wt % Al_2O_3 are also closely approached at these conditions (Figs 6 and 8a). In combination, we therefore take the intermediate plagioclase, clinopyroxene, amphibole, and magnetite compositions to estimate that the XH_2O_V and melt H_2O content of the recharge magma were ≥0·8 and ~4–5 wt %, and we infer that its temperature was >950 and <1000°C (Fig. 12c and d).

It is notable in this regard that H_2O-rich glass inclusions in natural samples from Merapi, which are inferred to represent, or closely approach, entrapment compositions, have up to ~5 wt % H_2O and ≤800 ppm CO_2 (Preece *et al.*, 2014). These inclusions with ≥2·5 wt % H_2O have compositions indicating equilibration with a vapour phase characterized by an XH_2O_V of between ~0·6 and ~0·8 (Fig. 11a; data from Preece *et al.*, 2014). This variation in glass H_2O and CO_2 contents and XH_2O_V could reflect the following: (1) analytical uncertainties; (2) analysis of compositionally heterogeneous glass domains and/or micron or submicron volatile inclusions [as proposed by Preece *et al.* (2014) for their CO_2-rich, but not for their H_2O-rich glass inclusion data]; (3) melt inclusions (glass) that variably re-equilibrated (leaked) during magma ascent. However, the compositional variation may also record the primary variations in melt composition and XH_2O_V that we infer on the basis of plagioclase and clinopyroxene compositions; that is, melt entrapment during inter-eruptive magma residence in equilibrium with an XH_2O_V of ~0·6 and melt entrapment during pre-eruptive magma recharge in equilibrium with an XH_2O_V of ~0·8 (Fig. 12).

Origin of the inferred volatile variation in Merapi's pre-eruptive magma reservoir

Our experimental study indicates that the Merapi pre-eruptive magma reservoir is contained within carbonate-dominated strata; previous experimental studies have characterized the release of CO_2 by carbonate assimilation in Merapi magmas (Deegan *et al.*, 2010; Blythe *et al.*, 2015). High $\delta^{13}C$ (CO_2) gas emissions from summit fumaroles during Merapi's eruption in 2006 have been interpreted as evidence for carbonate assimilation (Troll *et al.*, 2012), which at that time may have contributed significant amounts of CO_2 to Merapi's volatile budget. High CO_2 emissions prior to the 2010 eruption may also reflect CO_2 liberated by carbonate assimilation (Borisova *et al.*, 2013; Blythe *et al.*, 2015), but they may equally reflect CO_2 released from the recharge magmas (Surono *et al.*, 2012; Costa *et al.*, 2013). Phenocryst glass inclusions with high CO_2 contents may furthermore record CO_2 fluxing related to carbonate assimilation (Deegan *et al.*, 2010; Nadeau *et al.*, 2013; Blythe *et al.*, 2015), but the locally high CO_2 contents of glass inclusions trapped in Merapi's phenocrysts are more likely to represent heterogeneous post-entrapment CO_2 distribution (Preece *et al.*, 2014). In agreement with others, we therefore propose that Merapi's volatile phase comprises contributions from the carbonate-dominated upper crust, but that its largely uniform composition predominantly derives from a steady-state magma source comprising mantle and subducted sediment components (Allard, 1983, 2013; Allard *et al.*, 2011; Troll *et al.*, 2012).

That gas fluxing or degassing within Merapi's magma plumbing system accounts for most of the variations in XH_2O_V in the pre-eruptive reservoir is hence the most likely scenario. One possibility is that magmas reach Merapi's pre-eruptive reservoir with an XH_2O_V of ≥0·8 (Fig. 12). During storage they are then fluxed by CO_2-rich volatiles from deeper levels of the magma system, decreasing the reservoir's XH_2O_V to ~0·5–0·6 (Fig. 12c). Such CO_2-rich volatile fluxing of shallow reservoirs has been inferred for a number of arc volcanoes, including Mount St Helens and Soufrière Hills (Blundy *et al.*, 2010; Cashman & Blundy, 2013; Cassidy *et al.*, 2015; Riker *et al.*, 2015). For the Merapi system this process would require that CO_2 fluxing of the pre-eruptive reservoir is spatially fairly homogeneous, given that the largest phenocryst and microphenocryst volume crystallizes at these conditions. The characteristic plateau zones of clinopyroxene and plagioclase phenocrysts would further require that the reservoir's XH_2Ov reaches a steady state at ~0·5–0·6, which could indicate that the inflowing vapour is close to this composition or

that the influx of CO_2-rich vapour diminishes or ceases once the volatile phase of the pre-eruptive reservoir has reached this composition. In this scenario, Merapi's deeper magma plumbing system behaves as an open system, releasing volatiles, whereas the pre-eruptive reservoir behaves as a closed or semi-closed system during inter-eruptive periods, trapping some (or the majority) of the volatiles derived from deeper levels (Fig. 12c).

Another possible scenario is that magmas ascending through Merapi's magma supply system follow different degassing paths—open, vapour-buffered and closed-system degassing paths—during inter-eruptive and pre-eruptive recharge of the reservoir. During inter-eruptive periods, magmas reach the pre-eruptive reservoir with an XH_2O_V of ~0·5–0·6 (Fig. 12), following or approaching a vapour-buffered degassing path, along which both H_2O and CO_2 partially exsolve. During pre-eruptive recharge, in contrast, magmas ascend into Merapi's pre-eruptive reservoir following or approaching an open-system degassing path, releasing a comparatively large amount of CO_2, and thus reaching the reservoir at a higher XH_2O_V of ~0·8 (Fig. 12d). A comparable, although longer-term switch from closed-system to vapour-buffered degassing paths has been inferred for magmas that sourced the 1980 Mount St Helens' plinian eruption and its subsequent effusive 1980–1986 eruptions on the basis of both mineral assemblages and glass inclusion CO_2 and H_2O compositions (Blundy *et al.*, 2010; Riker *et al.*, 2015). That the supply system of Merapi's pre-eruptive reservoir has switched between degassing trends in such a fashion prior to 2010 and other recent eruptions (as recorded by equivalent mineral compositions and zoning patterns) could relate to changes in the magma ascent and supply rate, which ultimately trigger Merapi's small-volume eruptions. We consider this scenario plausible, because it is consistent with all the petrological and compositional data available, and because it can also account for the strong degassing of CO_2 observed prior to the onset of the 2010 eruption (e.g. Surono *et al.*, 2012). However, additional glass and fluid inclusion data and analyses of inter-eruptive and pre-eruptive gas emission data are urgently needed to further evaluate the inferred variation of volatile compositions and the proposed scenarios for volatile evolution.

CONCLUSIONS

The key findings of our study on pyroclasts erupted at Merapi, Indonesia, in 2010, and our experiments on one of its crystal-rich basaltic andesites are as follows.

1. Experiments that partially melt and partially recrystallize coarse-grained powders can constrain the crystallization conditions for both resident and recharge magmas in mixed systems by reconstructing local equilibrium conditions between mineral rim and host melt composition, if both magmas and their melt fractions are closely comparable in composition. The performance of standard crystallization experiments that reconstruct mineral and melt compositions at total equilibrium for the same starting material, and thus for a system with a similar composition, can be used to ascertain that the phase compositions produced in the melting experiments indeed represent local equilibrium.
2. Mount Merapi's current pre-eruptive reservoir hosts crystal-rich magma that is repeatedly recharged by basaltic andesite magma with a closely corresponding composition. The magmas partially crystallize at $\geq$100–200 $\pm$ 75 MPa and thus at a depth between *c.* 4·5 and 9 km. They are stored at ~925–950 $\pm$ 25°C with melt H_2O contents of ~3–4 wt %, and an XH_2O_V of ~0·5–0·6. Recharge magmas that mix with the resident magma of the reservoir have higher melt H_2O contents of ~4–5 wt %, a higher XH_2O_V of ~0·8, and a higher temperature of >950 to <1000°C. These variations in melt H_2O and XH_2O_V of the resident and recharge magmas may reflect variable degrees of open-system degassing of the magmas en route to the pre-eruptive magma storage reservoir, which may in turn record variations in magma ascent and supply rates from the deep plumbing system.

FUNDING

This research was funded by the DOMERAPI ANR project (ANR- 12-BS06-0012) of the French Agence Nationale pour la Recherche awarded to J.-P. Métaxian and co-workers. The analysis of deposits and the reconstruction of the eruption chronology was achieved by partial funding to J.C.K. from the CASAVA ANR-09-RISK-002 project.

ACKNOWLEDGEMENTS

We are grateful to RISTEK for allowing us to undertake this research and to the Yogyakarta Special Territory for administrative support. We thank Dr Surono, Dr Hendrasto (PVMBG/CVGHM), and Dr Subandryio (BPPTKG) for their steadfast support, and our Indonesian colleagues for field and administrative assistance. We are very grateful to J-P. Toutain and Etny at IRD for their valuable assistance and institutional support. We are most indebted to Sofie and her staff at PVMBG for help with administrative procedures. We would like to thank our DOMERAPI colleagues for many discussions, J. Andújar and G. Iacono-Marziano for help with the experiments, and I. Di Carlo for assistance with SEM imaging and microprobe analyses. Special thanks go to Svetlana Byrdina, who collected the stage 7 samples for us. Thoughtful and constructive reviews by J. Barclay, R. B. Stewart and an anonymous reviewer, and the editorial support of R. Price and A. Lumsden are much appreciated.

SUPPLEMENTARY DATA

Supplementary data for this paper are available at *Journal of Petrology* online.

REFERENCES

Abdurachman, E. K. (1998). Géologie des produits de l'activité historique et contribution à l'évaluation des risques au Merapi (Java), Indonésie. PhD thesis, Université d'Orléans, 289 pp.

Allard, P. (1983). The origin of hydrogen, carbon, sulphur, nitrogen and rare gases in volcanic exhalations; evidence from isotope geochemistry. In: Tazieff, H. & Sabroux, J. (eds) *Forecasting Volcanic Events*. Elsevier, pp. 337–386.

Allard, P. (2013). Isotopic and mass balance constraints on the origin(s) of carbon dioxide emissions from Merapi volcano, central Java, Indonesia. *IAVCEI Scientific Assembly Abstracts* 1P2_3J–O10.

Allard, P., Métrich, N. & Sabroux, J.-C. (2011). Volatile and magma supply to standard eruptive activity at Merapi volcano, Indonesia. *Geophysical Research Abstracts* **13**, EGU2011–13522.

Alonso-Perez, R., Müntener, O. & Ulmer, P. (2009). Igneous garnet and amphibole fractionation in the roots of island arcs: experimental constraints on andesitic liquids. *Contributions to Mineralogy and Petrology* **157**, 541–558.

Andreastuti, S. D., Alloway, B. V. & Smith, I. E. M. (2000). A detailed tephrostratigraphic framework at Merapi Volcano, Central Java, Indonesia: implications for eruption predictions and hazard assessment. *Journal of Volcanology and Geothermal Research* **100**, 51–67.

Baker, D. R. & Alletti, M. (2012). Fluid saturation and volatile partitioning between melts and hydrous fluids in crustal magmatic systems: the contribution of experimental measurements and solubility models. *Earth-Science Reviews* **114**, 298–324.

Barclay, J. & Carmichael, I. S. E. (2004). A hornblende basalt from western Mexico: Water-saturated phase relations constrain a pressure–temperature window of eruptibility. *Journal of Petrology* **45**, 485–506.

Beauducel, F. & Cornet, F. H. (1999). Collection and three-dimensional modeling of GPS and tilt data at Merapi volcano, Java. *Journal of Geophysical Research* **104**, 725–736.

Berlo, K., Blundy, J., Turner, S. & Hawkesworth, C. (2007). Textural and chemical variation in plagioclase phenocrysts from the 1980 eruptions of Mount St. Helens, USA. *Contributions to Mineralogy and Petrology* **154**, 291–308.

Berthommier, P. C. (1990). Etude volcanologique du Merapi (Centre-Java), tephrostratigraphie et chronologie—produits eruptifs. PhD thesis, Universite Blaise Pascal, Clermont-Ferrand, 216 pp.

Blatter, D. L., Sisson, T. W. & Hankins, W. B. (2013). Crystallization of oxidized, moderately hydrous arc basalt at mid- to lower-crustal pressures: implications for andesite genesis. *Contributions to Mineralogy and Petrology* **166**, 861–886.

Blundy, J. & Cashman, K. (2008). Petrologic reconstruction of magmatic system variables and processes. In: Putirka, K. D. & Tepley, F. J., III (eds) *Minerals, Inclusions and Volcanic Processes. Mineralogical Society of America and Geochemical Society, Reviews in Mineralogy and Geochemistry* **69**, 179–239.

Blundy, J., Cashman, K. V., Rust, A. & Witham, F. (2010). A case for CO_2-rich arc magmas. *Earth and Planetary Science Letters* **290**, 289–301.

Blythe, L. S., Deegan, F. M., Freda, C., Jolis, E. M., Masotta, M., Misiti, V., Taddeucci, J. & Troll, V. R. (2015). CO_2 bubble generation and migration during magma–carbonate interaction. *Contributions to Mineralogy and Petrology* **169**, 42.

Bogaerts, M., Scaillet, B. & Vander Auwera, J. (2006). Phase equilibria of the Lyngdal granodiorite (Norway): Implications for the origin of metaluminous ferroan granitoids. *Journal of Petrology* **47**, 2405–2431.

Borisova, A. Y., Martel, C., Gouy, S., Pratomo, I., Sumarti, S., Toutain, J.-P., Bindeman, I. N., de Parseval, P., Metaxian, J.-P. & Surono (2013). Highly explosive 2010 Merapi eruption: evidence for shallow-level crustal assimilation and hybrid fluid. *Journal of Volcanology and Geothermal Research* **261**, 193–208.

Budi-Santoso, A., Lesage, P., Dwiyono, S., Sumarti, S., Subandriyo, J., Surono, Jousset, P. & Metaxian, J.-P. (2013). Analysis of the seismic activity associated with the 2010 eruption of Merapi volcano, Java. *Journal of Volcanology and Geothermal Research* **261**, 153–170.

Camus, G., Gourgaud, A., Mossand-Berthommier, P.-C. & Vincent, P. M. (2000). Merapi (Central Java, Indonesia): an outline of the structural and magmatological evolution, with a special emphasis to the major pyroclastic events. *Journal of Volcanology and Geothermal Research* **100**, 139–163.

Caricchi, L., Ulmer, P. & Peccerillo, A. (2006). A high-pressure experimental study on the evolution of the silicic magmatism of the Main Ethiopian Rift. *Lithos* **91**, 46–58.

Cashman, K. & Blundy, J. (2013). Petrological cannibalism: the chemical and textural consequences of incremental magma body growth. *Contributions to Mineralogy and Petrology* **166**, 703–729.

Cashman, K. V. & Sparks, R. S. J. (2013). How volcanoes work: A 25 year perspective. *Geological Society of America Bulletin* **125**, 664–690.

Cassidy, M., Edmonds, M., Watt, S. F. L., Palmer, M. R, & Gernon, T. M. (2015). Origin of basalts by hybridization in andesite-dominated arcs. *Journal of Petrology* **56**, 1–22.

Chadwick, J. P., Troll, V. R., Ginibre, C., Morgan, D., Gertisser, R., Waight, T. E. & Davidson, J. P. (2007). Carbonate assimilation at Merapi Volcano, Java, Indonesia: insights from crystal isotope stratigraphy. *Journal of Petrology* **48**, 1793–1812.

Chadwick, J. P., Troll, V. R., Waight, T. E., van der Zwan, F. M. & Schwarzkopf, L. M. (2013). Petrology and geochemistry of igneous inclusions in recent Merapi deposits: a window into the sub-volcanic plumbing system. *Contributions to Mineralogy and Petrology* **165**, 259–282.

Charbonnier, S. & Gertisser, R. (2008). Field observations and surface characteristics of pristine block-and-ash flow deposits from the 2006 eruption of Merapi Volcano, Java, Indonesia. *Journal of Volcanology and Geothermal Research* **177**, 971–982.

Charbonnier, S. J., Germa, A. M., Connor, C. B., Gertisser, R., Preece, K., Komorowski J.-C., Lavigne, F., Dixon, T. H. & Connor, L. J. (2013). Evaluation of the impact of the 2010 pyroclastic density currents at Merapi volcano from high-resolution satellite imagery analysis, field investigations and numerical simulations. *Journal of Volcanology and Geothermal Research* **261**, 295–315.

Costa, F., Scaillet, B. & Pichavant, M. (2004). Petrological and experimental constraints on the pre-eruption compositions of Holocene dacite from Volcàn San Pedro (36°S, Chilean Andes) and importance of sulphur in silicic subduction-related magmas. *Journal of Petrology* **45**, 855–881.

Costa, F., Andreastuti, S., Bouvet de Maisonneuve, C. & Pallister, J. S. (2013). Petrological insights into the storage conditions, and magmatic processes that yielded the

centennial 2010 Merapi explosive eruption. *Journal of Volcanology and Geothermal Research* **261**, 209–235.

Deegan, F. M., Troll, V. R., Freda, C., Misiti, V., Chadwick, J. P., McLeod, C. L. & Davidson, J. P. (2010). Magma–Carbonate interaction processes and associated CO^2 release at Merapi Volcano, Indonesia: insights from experimental petrology. *Journal of Petrology* **51**, 1027–1051.

Dungan, M. A., Wulff, A. & Thompson, R. (2001). Eruptive stratigraphy of the Tatara–San Pedro complex, 36°S, Southern Volcanic Zone, Chilean Andes: Reconstruction method and implications for magma evolution at longlived arc volcanic centers. *Journal of Petrology* **42**, 555–626.

Erdmann, S., Martel, C., Pichavant, M. & Kushnir, A. (2014). Amphibole as an archivist of magmatic crystallization conditions: problems, potential, and implications for inferring magma storage prior to the paroxysmal 2010 eruption of Mount Merapi, Indonesia. *Contributions to Mineralogy and Petrology* **167**, 1016–1038.

Foley, F. V., Pearson, N. J., Rushmer, T., Turner, S. & Adam, J. (2013). Magmatic evolution and magma mixing of Quaternary adakites at Solander and Little Solander Islands, New Zealand. *Journal of Petrology* **54**, 703–744.

Genareau, K., Cronin, S. J. & Lube, G. (2014). Effects of volatile behaviour on dome collapse and resultant pyroclastic surge dynamics: Guning Merapi 2010 eruption. In: Zellmer, G. F., Edmonds, M. & Straub, S. M. (eds) *The Role of Volatiles in the Genesis, Evolution and Eruption of Arc Magmas. Geological Society, London, Special Publications* **410**, 199–218.

Gertisser, R. (2001). Gunung Merapi (Java, Indonesien): Eruptionsgeschichte und Magmatische Evolution eines Hochrisiko-Vulkans. PhD thesis, Universität Freiburg, 382 pp.

Gertisser, R., Charbonnier, S. J., Troll, V. R., Keller, J., Preece, K., Chadwick, J. P. & Herd, R. A. (2011). Merapi (Java, Indonesia): anatomy of a killer volcano. *Geology Today* **27**, 57–62.

Gertisser, R. & Keller, J. (2003). Trace element and Sr, Nd, Pb and O isotope variations in medium-K and high-K volcanic rocks from Merapi Volcano, Central Java, Indonesia: evidence for the involvement of subducted sediments in Sunda Arc Magma Genesis. *Journal of Petrology* **44**, 457–489.

Grove, T. L., Elkins-Tanton, L. T., Parman, S. W., Chatterjee, N., Müntener, O. & Gaetani, G. A. (2003). Fractional crystallization and mantle-melting controls on calc-alkaline differentiation trends. *Contributions to Mineralogy and Petrology* **145**, 515–533.

Jousset, P., Budi-Santoso, A., Jolly, A. D., Boichu, M., Surono, Dwiyono, S., Sumatri, S., Hidayati, S. & Thierry, P. (2013). Signs of magma ascent in LP and VLP seismic events and link to degassing: an example from the 2010 explosive eruption at Merapi volcano, Indonesia. *Journal of Volcanology and Geothermal Research* **261**, 171–192.

Kiss, B., Harangi, S., Ntaflos, T., Mason, P. R. D. & Pál-Molnár, E. (2014). Amphibole perspective to unravel pre-eruptive processes and conditions in volcanic plumbing systems beneath intermediate arc volcanoes: a case study from Ciomadul volcano (SE Carpathians). *Contributions to Mineralogy and Petrology* **167**, 986.

Komorowski, J.-C., Jenkins, S., Baxter, P. J., Picquout, A., Lavigne, F., Charbonnier, S., Gertisser, R., Noer, C., Budi-Santoso, A. & Surono (2013). Paroxysmal dome explosion during the Merapi 2010 eruption: processes and facies relationships of associated high-energy pyroclastic density currents. *Journal of Volcanology and Geothermal Research* **261**, 260–294.

Krawczynski, M. J., Grove, T. L. & Behrens, H. (2012). Amphibole stability in primitive arc magmas: effects of temperature, H_2O content, and oxygen fugacity. *Contributions to Mineralogy and Petrology* **164**, 317–339.

Martel, C., Pichavant, M., Holtz, F., Scaillet, B., Bourdier, J.-L. & Traineau, H. (1999). Effects of fO_2 and H_2O on andesite phase relations between 2 and 4 kbar. *Journal of Geophysical Research* **104**, 29453–29470.

Mercer, C. N. & Johnston, A. D. (2008). Experimental studies of the *P–T*–H_2O near-liquidus phase relations of basaltic andesite from North Sister Volcano, high Oregon Cascades: constraints on lower-crustal mineral assemblages. *Contributions to Mineralogy and Petrology* **155**, 571–592.

Moore, G. & Carmichael, I. S. E. (1998). The hydrous phase equilibria (to 3 kbar) of an andesite and basaltic andesite from western Mexico: constraints on water content and conditions of phenocryst growth. *Contributions to Mineralogy and Petrology* **130**, 304–319.

Müller, A. & Haak, V. (2004). 3-D modelling of a conductivity structure: Integrating magnetotellurics, induction vectors and the effect of steep topography—A case study from Merapi volcano (Central Java). *Journal of Volcanology and Geothermal Research* **138**, 205–222.

Murphy, M. D., Sparks, R. S. J., Barclay, J., Carroll, M. R. & Brewer, T. S. (2000). Remobilization of andesite magma by intrusion of mafic magma at the Soufrière Hills Volcano, Montserrat, West Indies. *Journal of Petrology* **1**, 21–42.

Nadeau, O., Williams-Jones, A. E. & Stix, J. (2010). Sulphide magma as a source of metals in arc-related magmatic hydrothermal ore fluids. *Nature Geoscience* **3**, 501–505.

Nadeau, O., Williams-Jones, A. E. & Stix, J. (2013). Magmatic–hydrothermal evolution and devolatilization beneath Merapi volcano, Indonesia. *Journal of Volcanology and Geothermal Research* **261**, 50–68.

Nandedkar, R. H., Ulmer, P. & Müntener, O. (2014). Fractional crystallization of primitive, hydrous arc magmas: an experimental study at 0·7 GPa. *Contributions to Mineralogy and Petrology* **167**, 1015.

Newman, S. & Lowenstern, J. B. (2002). VOLATILECALC: a silicate melt–H_2O–CO_2 solution model written in Visual Basic for Excel. *Computers and Geosciences* **28**, 597–604.

Nimis, P. (1999). Clinopyroxene geobarometry of magmatic rocks. Part 2. Structural geobarometers for basic to acid, tholeiitic and mildly alkaline magmatic systems. *Contributions to Mineralogy and Petrology* **135**, 62–74.

Parman, S. W., Grove, T. L., Kelley, K. A. & Plank, T. (2011). Along-arc variations in the pre-eruptive H_2O contents of Mariana arc magmas inferred from fractionation paths. *Journal of Petrology* **52**, 257–278.

Picard, C., Monzier, M., Eissen, J.-P. & Robin, C. (1994). Concomitant evolution of tectonic environment and magma geochemistry, Ambrym volcano (Vanuatu, New Hebrides arc). In: Smellie, J. L. (ed.) *Volcanism Associated with Extension at Consuming Plate Margins. Geological Society, London, Special Publications* **81**, 135–154.

Pichavant, M., Martel, C., Bourdier, J.-L. & Scaillet, B. (2002). Physical conditions, structure and dynamics of a zoned magma chamber: Mt. Pelée (Martinique, Lesser Antilles Arc). *Journal of Geophysical Research* **107**, doi:org/10.1029/2001JB000315.

Pichavant, M., Costa, F., Burgisser, A., Scaillet, B., Martel, C. & Poussineau, S. (2007). Equilibration scales in silicic to intermediate magmas—implications for experimental studies. *Journal of Petrology* **48**, 1955–1972.

Pietranik, A., Holtz, F., Koepke, J. & Puziewicz, J. (2009). Crystallization of quartz dioritic magmas at 2 and 1 kbar: experimental results. *Mineralogy and Petrology* **97**, 1–21.

Pownceby, M. I. & O'Neill, H. St. C. (1994). Thermodynamic data from redox reactions at high temperatures. III. Activity–

composition relations in Ni–Pd alloys from EMF measurements at 850–1250 K, and calibration of the NiO + Ni–Pd assemblage as a redox sensor. *Contributions to Mineralogy and Petrology* **116**, 327–339.

Preece, K., Barclay, J., Gertisser, R. & Herd, R. A. (2013). Textural and micro-petrological variations in the eruptive products of the 2006 dome-forming eruption of Merapi volcano, Indonesia: implications for sub-surface processes. *Journal of Volcanology and Geothermal Research* **261**, 98–120.

Preece, K., Gertisser, R., Barclay, J., Berlo, K., Herd, R. A. & Edinburgh Ion Microprobe Facility (2014). Pre- and syn-eruptive degassing and crystallisation processes of the 2010 and 2006 eruptions of Merapi volcano, Indonesia. *Contributions to Mineralogy and Petrology* **168**, 1061.

Prouteau, G. & Scaillet, B. (2003). Experimental constraints on the origin of the 1991 Pinatubo dacite. *Journal of Petrology* **44**, 2203–2241.

Putirka, K. D. (2008). Thermometers and barometers for volcanic systems. In: Putirka, K. D. & Tepley, F. J., III (eds) *Minerals, Inclusions and Volcanic Processes. Mineralogical Society of America and Geochemical Society, Reviews in Mineralogy and Geochemistry* **69**, 61–120.

Putirka, K. D., Mikaelian, H., Ryerson, F. & Shaw, H. (2003). New clinopyroxene–liquid thermobarometers for mafic, evolved, and volatile-bearing lava compositions, with applications to lavas from Tibet and the Snake River Plain, Idaho. *American Mineralogist* **88**, 1542–1554.

Ratdomopurbo, A. & Poupinet, G. (1995). Monitoring a temporal change of seismic velocity in a volcano: application to the 1992 eruption of Mt Merapi (Indonesia). *Geophysical Research Letters* **22**, 775–778.

Ratdomopurbo, A. & Poupinet, G. (2000). An overview of the seismicity of Merapi volcano (Java, Indonesia), 1983–1994. *Journal of Volcanology and Geothermal Research* **100**, 193–214.

Ridolfi, F. & Renzulli, A. (2012). Calcic amphiboles in calc-alkaline and alkaline magmas: thermobarometric and chemometric empirical equations valid up to 1130°C and 2·2 GPa. *Contributions to Mineralogy and Petrology* **163**, 877–895.

Ridolfi, F., Renzulli, A. & Puerini, M. (2010). Stability and chemical equilibrium of amphibole in calc-alkaline magmas: an overview, new thermobarometric formulations and application to subduction-related volcanoes. *Contributions to Mineralogy and Petrology* **160**, 45–66.

Riker, J. M., Blundy, J. D., Rust, A. C., Botcharnikov, R. E. & Humphreys, M. C. S. (2015). Experimental phase equilibria of a Mount St. Helens rhyodacite: a framework for interpreting crystallization paths in degassing silicic magmas. *Contributions to Mineralogy and Petrology* **170**, 6, doi: 10.1007/s00410-015-1160-5.

Ruprecht, P. & Bachmann, O. (2010). Pre-eruptive reheating during magma mixing at Quizapu volcano and the implications for the explosiveness of silicic arc volcanoes. *Geology* **38**, 919–922.

Saepuloh, A., Koike, K., Omura, M., Iguchi, M. & Setiawan, A. (2010). SAR and gravity change-based characterization of the distribution pattern of pyroclastic flow deposits at Mt. Merapi during the past 10 years. *Bulletin of Volcanology* **72**, 221–232.

Scaillet, B. & Evans, B. (1999). The 15 June 1991 eruption of Mount Pinatubo. I. Phase equilibria and pre-eruption *P–T–f*H2O–*f*O2 conditions of the dacite magma. *Journal of Petrology* **40**, 381–411.

Scaillet, B., Pichavant, M. & Cioni, R. (2008). Upward migration of Vesuvius magma chamber over the past 20,000 years. *Nature* **455**, 216–219.

Sisson, T. W. & Grove, T. L. (1992). Experimental investigations of the role of H_2O in calc-alkaline differentiation and subduction zone magmatism. *Contributions to Mineralogy and Petrology* **113**, 143–166.

Sisson, T. W. & Grove, T. L. (1993). Temperatures and H_2O contents of low-MgO high-alumina basalts. *Contributions to Mineralogy and Petrology* **113**, 167–184.

Smyth, H. R., Hall, R., Hamilton, J. & Kinny, P. (2005). East Java: Cenozoic basins, volcanoes and ancient basement. *Proceedings, Indonesian Petroleum Association. Thirtieth Annual Convention and Exhibition Proceedings* 251–266.

Sparks, R. S. J. (2003). Forecasting volcanic eruptions. *Earth and Planetary Science Letters* **210**, 1–15.

Stamper, C. C., Blundy, J. D., Arculus, R. J. & Melekhova, E. (2014). Petrology of plutonic xenoliths and volcanic rocks from Grenada, Lesser Antilles. *Journal of Petrology* **55**, 1353–1387.

Streck, M. J., Broderick, C. A., Thornber, C. R., Clynne, M. A. & Pallister, J. S. (2008). Plagioclase populations and zoning in dacite of the 2004–2005 Mount St. Helens eruption: constraints for magma origin and dynamics. In: Sherrod, D. R., Scott, W. E. & Stauffer, P. H. (eds) *A Volcano Rekindled; the Renewed Eruption of Mount St. Helens, 2004–2006. US Geological Survey, Professional Papers* **1750**, 791–808.

Surono, Jousset, P., Pallister, J., Boichu, M., Buongiorno, M. F., Budisantoso, A., Costa, F., Andreastuti, S., Prata, F., Schneider, D., Clarisse, L., Humaida, H., Sumarti, S., Bignami, C., Griswold, J., Carn, S., Oppenheimer, C. & Lavigne, F. (2012). The 2010 explosive eruption of Java's Merapi volcano—A '100-year' event. *Journal of Volcanology and Geothermal Research* **241–242**, 121–135.

Tiede, C., Camacho, A. G., Gerstenecker, C., Fernandez, J. & Suyanto, I. (2005). Modeling the density at Merapi volcano area, Indonesia, via the inverse gravimetric problem. *Geochemistry, Geophysics, Geosystems* **6**, http://dx.doi.org/10.1029/2005GC000986.

Troll, V. R., Hilton, D. R., Jolis, E. M., Chadwick, J. P., Blythe, L. S., Deegan, F. M., Schwarzkopf, L. M. & Zimmer, M. (2012). Crustal CO_2 liberation during the 2006 eruption and earthquake events at Merapi volcano, Indonesia. *Geophysical Research Letters* **39**, L11302, doi:10.1029/2012GL051307.

Troll, V. R., Deegan, F. M., Jolis, E. M., Harris, C., Chadwick, J. P., Gertisser, R., Schwarkopf, L. M., Borisova, A. Y., Bindeman, I. N., Sumarti, S. & Preece, K. (2013). Magmatic differentiation processes at Merapi volcano: inclusion petrology and oxygen isotopes. *Journal of Volcanology and Geothermal Research* **261**, 38–49.

Turner, M. B., Cronin, S. J., Stewart, R. B., Bebbington, M. & Smith, I. E. M. (2008). Using titanomagnetite textures to elucidate volcanic eruption histories. *Geology* **36**, 31–34.

Van der Zwan, F. M., Chadwick, J. P. & Troll, V. R. (2013). Textural history of recent basaltic-andesites and plutonic inclusions from Merapi volcano. *Contributions to Mineralogy and Petrology* **166**, 43–63.

Voight, B., Constantine, E. K., Sismowidjoyo, S. & Torley, R. (2000). Historical eruptions of Merapi volcano, Central Java, Indonesia, 1768–1998. *Journal of Volcanology and Geothermal Research* **100**, 69–138.

Whitney, D. L. & Evans, B. W. (2010). Abbreviations for names of rock-forming minerals. *American Mineralogist* **95**, 185–187.

Woods, A. W. (1995). The dynamics of explosive volcanic eruptions. *Reviews of Geophysics* **33**, 495–530.